AD A053654

Estimates From Satellites of Weather Erosion Parameters for Reentry Systems

JOHN H. CONOVER
JAMES T. BUNTING

29 November 1977

DDC
MAY 9 1978
F

METEOROLOGY DIVISION   PROJECT 627A

# AIR FORCE GEOPHYSICS LABORATORY

HANSCOM AFB, MASSACHUSETTS 01731

AIR FORCE SYSTEMS COMMAND, USAF

This report has been reviewed by the ESD Information Office (OI) and is releasable to the National Technical Information Service (NTIS).

This technical report has been reviewed and is approved for publication.

FOR THE COMMANDER

Chief Scientist

SECURITY CLASSIFICATION OF THIS PAGE (When Data Entered)

REPORT DOCUMENTATION PAGE	READ INSTRUCTIONS BEFORE COMPLETING FORM

1. REPORT NUMBER	2. GOVT ACCESSION NO.	3. RECIPIENT'S CATALOG NUMBER
AFGL-TR-77-0260 *AFGL-AFSG-377*		

4. TITLE (and Subtitle)	5. TYPE OF REPORT & PERIOD COVERED
ESTIMATES FROM SATELLITES OF WEATHER EROSION PARAMETERS FOR REENTRY SYSTEMS	
	6. PERFORMING ORG. REPORT NUMBER AFSG No. 377

7. AUTHOR(s)	8. CONTRACT OR GRANT NUMBER(s)
John H. Conover James T. Bunting	

9. PERFORMING ORGANIZATION NAME AND ADDRESS	10. PROGRAM ELEMENT, PROJECT, TASK AREA & WORK UNIT NUMBERS
Air Force Geophysics Laboratory (LYU) Hanscom AFB, Massachusetts 01731	63311F 627A0003

11. CONTROLLING OFFICE NAME AND ADDRESS	12. REPORT DATE
Air Force Geophysics Laboratory (LYU) Hanscom AFB, Massachusetts 01731	29 Nov 1977
	13. NUMBER OF PAGES 85 84 p.

14. MONITORING AGENCY NAME & ADDRESS(if different from Controlling Office)	15. SECURITY CLASS. (of this report)
	Unclassified
	15a. DECLASSIFICATION/DOWNGRADING SCHEDULE

16. DISTRIBUTION STATEMENT (of this Report)

Approved for public release; distribution unlimited.

17. DISTRIBUTION STATEMENT (of the abstract entered in Block 20, if different from Report)

16 627A   17 DD

18. SUPPLEMENTARY NOTES

Air Force surveys in geophysics

19. KEY WORDS (Continue on reverse side if necessary and identify by block number)

Weather satellites	Clouds	Reentry systems
Infrared sensors	Cloud ice	Material erosion
Visible sensors	Cloud water	Weather erosion
Hydrometeors	Cloud mass	RV recession
Precipitation	Aircraft cloud sensing	RV range errors

20. ABSTRACT (Continue on reverse side if necessary and identify by block number)

A final report on satellite correlation studies supporting the SAMSO ABRES program is given. Techniques to estimate reentry vehicle weather erosion parameters from satellite measurements are described. The techniques were developed over a period of three years. An empirical approach was followed with simultaneous measurements of clouds by aircraft and satellite sensors in a series of 41 cases covering a great range of cloud conditions. For each case the aircraft measurements of clouds supplemented by surface weather reports and radar pictures were converted to profiles of hydrometeor densities vs

DD FORM 1 JAN 73 1473   EDITION OF 1 NOV 65 IS OBSOLETE

20.   (Cont)

altitude. One case, 8 October 1976, is described in detail and illustrates problems in the analysis of aircraft and satellite data.   Four different erosion parameters were calculated for all profiles. The erosion parameters predict the amount of material eroded from a nosetip and the range error of the re-entry system due to erosion by ice and water particles in the atmosphere.   The erosion parameters were related to infrared and visible satellite imagery data from NOAA ITOS satellites by means of non-linear equations.   Equations were also developed to estimate total cloud mass and thickness from the same satellite data. The visible data were normalized to approximate the reflection geometry of both sun and satellite directly over the cloud.   The areal mean temperature from the infrared imagery data was found to be the most significant single predictor for erosion parameters; however, the most accurate estimates of erosion parameters came from a combination of infrared and visible data.   Another set of equations was developed using only infrared data and climatological temperature altitude profiles, and these equations were used for areas without sunlight or with highly reflective snow cover.

Extensive applications and tests were made of the equations to estimate erosion parameters from satellite data. One year (April 1973 to March 1974) of data from NOAA polar-orbiting satellites was processed and climatologies of erosion parameters were produced for most of Eurasia and for test ranges at Wallops Island, VA, and at Kwajalein Atoll.   The prediction equations were adapted to infrared and visible data from geostationary satellites and real time estimates of erosion parameters were provided to the test ranges through the AFGL Man Computer Interactive Data Access System. The erosion predictions were tested with good results in a variety of approaches including a statistical study, an additional series of aircraft flights near Kwajalein, a comparison to radar estimates of weather erosion and also a comparison to subjective estimates of erosion based on standard weather reports.

Preface

The following report relies on measurements from complicated satellite and aircraft systems. Technique development and the resulting satellite estimates of reentry vehicle erosion would not have been possible without the assistance of many individuals and organizations. Aircraft sampling of clouds underneath satellite passes was directed by the Convective Cloud Physics Branch (LYC), AFGL, under Dr. Cunningham and later Dr. Barnes. Captains Brooks, Cameron, Delgago, Kelley and Lt. Col. Church served as flight directors for most of the missions. Additional flights were made under contract by Meteorology Research, Inc., and Aeromet, Inc. Aircraft data reduction was provided by Mr. Glass of LYC and by Digital Programming Services, Inc. Satellite data and much helpful discussion were provided by the National Environmental Satellite Service and National Climatic Center of NOAA. Helpful studies were provided by Mr. Cozzens and others of Regis College to display estimates of cloud properties derived from satellite data and apply the estimation techniques to geosynchronous data in the AFGL McIDAS system. Mr. Myers of LY and the McIDAS team directed the real time applications in this report. Ms. Bench, formerly of the Satellite Meteorology Branch, wrote most of the computer programs for the analysis of archived satellite data with assistance from Environmental Research and Technology, Inc. (ERT). Radar data were taken and analyzed by the Radar Meteorology Branch under Mr. Glover and by ERT. Important consultation was provided by Mr. Lund, Design Climatology, and by Dr. Cunningham, Senior Scientist in Cloud Physics. Finally, every step of the work by the authors was encouraged and assisted by Mr. Touart, Manager of the AFGL Weather Erosion Program.

3

Contents

Estimates From Satellites of Weather Erosion
Parameters for Reentry Systems

1. INTRODUCTION

1.1 The Significance of Weather Erosion

The nosetips of reentry vehicles are subjected to extremes of aerodynamic
heating and pressure while decelerating in the atmosphere. The air temperature
in the boundary layer often reaches values above 10,000°F, which, combined with
the surface shear forces, promotes intense convective heat transfer to the surface.
Nosetips made of material with high heats of ablation have been designed to provide
protection to the essential parts of the vehicle. The amount of nosetip material
required for heat protection during clear air reentry has been minimized due to
cost and weight considerations. Additional mass loss may occur due to hypervelo-
city impact with atmospheric hydrometeors. Additional nosetip material is re-
quired to assure vehicle protection margins are maintained. Unpredictable nose-
tip mass loss may also affect system targeting accuracy. The problem of hydro-
meteor erosion increases with velocity and must, therefore, be considered in the
design of high performance reentry systems.

Although hydrometeor erosion is only one constraint among many in the design
of reentry systems, it has been investigated extensively by the Advanced Ballistic
Reentry Systems (ABRES) program of the Air Force Space and Missiles Systems
Organization (SAMSO). Since 1973, ABRES, which is the DoD lead agency for the

design of reentry systems, has sponsored projects to develop climatologies of erosive weather over target areas. This report summarizes the results of the Satellite Correlation Study, which uses data from weather satellites to estimate the erosion potential of clouds over target areas. Useful by-products of this study are climatologies and real-time estimates of erosion potential at test ranges.

1.2 Previous Erosion Climatologies

Climatologies have been developed in three earlier studies. Theoretical and empirical methods to measure cloud and precipitation moisture were thoroughly reviewed by Smith,[1] who developed relationships to specify particle water or ice content at points in time and space. Feddes[2] applied these relationships to the USAF global 3DNEPH analysis output to produce estimates of condensed moisture content. AFGL experience with the results indicated occasional large inconsistencies with surface observations of precipitation, especially in the cold season. In addition, the vertical resolution of the upper layers was often too coarse for hydrometeor profiles suitable for erosion studies. In another climatology, known as AFGL I, moisture profiles were modeled from upper air (RAOB) and surface weather reports. The model was applied to selected RAOB stations in Europe and Asia. Like the Smith-Feddes model, it was entirely objective and computer compatible. A more detailed climatology, known as AFGL II, was developed by Cunningham and Peirce[3] and allowed for many subjective decisions. Time-height cross sections were prepared for 11 stations over a one-year period, February 1973 to January 1974. Preparation of the cross sections is described by Feteris, Lisa, and Bussey.[4] Data used were 3-hourly surface reports and 3DNEPH, 6-hourly RAOBS, 12-hourly surface maps and daily DMSP satellite high resolution imagery. The cross-sections represented a best possible cloud depiction prepared by experienced analysts. Cloud mass densities were then assigned using average values for cloud types and temperature modified according to system strengths and state of development or decay. Vertical profiles of mass density were recorded every 3 hours. The high frequency of profiles from this model was a distinct asset but its practical limitation to small "areas of representativeness" was a weakness. The

1. Smith, R.C., Capt (1974) Atmospheric Moisture Parameterization, USAFETAC TN 74-1, Washington, D.C. 19 pp.

2. Feddes, R.G., Capt (1974) A Synoptic-scale Model for Simulating Condensed Atmospheric Moisture, USAFETAC TN 74-1, Washington, D.C., 21 pp

3. Cunningham, R.M., and Peirce, R.M. (1974) Environmental Definition Plan Cross Section Analysis, AFGL (unpub. ms.).

4. Feteris, P.J., Lisa, A.S., and Bussey, A.J. (1975) Environmental Definition Program Cross Sectional Analysis; Summary of Data and Analysis Techniques, AFCRL-TR-76-0002. Final Rept. F19628-74-C-0073, Environmental Res. and Tech., Inc., Concord, Massachusetts 01742, 34 pp.

limitations were addressed by Gringorten[5] who developed stochastic models for approximating the occurrence of weather events various distances from the point of the event.

1.3 The Utility of Satellite Data

In the Satellite Correlation Study, infrared and visible satellite data have been used to estimate erosion parameters directly, rather than the vertical profile of hydrometeor mass density. The erosion parameters are weighted integrals of the density profiles which estimate total erosion or range foreshortening. Estimates have been calculated once per day for one year (April 1973 to March 1974) over all of Europe and Asia and for test ranges at Kwajalein and Wallops Island.

The satellite estimates have some advantages when compared to the earlier studies. First of all, the satellite estimates provide areal coverage information so that it is known when widely separated targets are simultaneously covered by erosive clouds. Second, the estimates do not rely on data from foreign weather services but use data from USA satellites. Third, the satellite estimates are sensitive to the upper regions of clouds, which account for much of the nosetip erosion and are not well described by conventional weather data. Finally, the satellite data and computational techniques lend themselves to computer processing and real-time applications. Computer processing is a distinct advantage in dealing with vast areas of Europe and Asia once per day for one year. Real-time applications proved useful in short term forecasts for the Wallops Island Range and the Kwajalein Missile Range, since there are few reports of cloud systems over water.

1.4 Related Satellite Studies

Recent publications in satellite meteorology and in the radiative properties of clouds have been reviewed for sources of input to weather erosion requirements. The requirements are severe. The most useful information for nosetip erosion models is the vertical profile of hydrometeor mass density. It is extremely unlikely, however, that detailed vertical profiles could be inferred from present satellite measurements since present sensors are passive instruments recording reflected sunlight or thermal emission from clouds. The sensors are sensitive to the optical depths of clouds, which do not bear a one-to-one correspondence with vertical profiles of cloud mass since many different profiles could have the same optical depth. Consequently, it is not surprising that there have been no studies to retrieve detailed vertical profiles of cloud mass.

---

5. Gringorten, I.I. (1976) Areal Coverage Estimates by Stochastic Modeling, AFGL-TR-76-0148, ERP No. 573, 56 pp.

11

Fortunately, estimates of integrated profiles of hydrometeor mass density are also useful for nosetip erosion studies and satellite measurements are useful for estimating integrated profiles. In research sponsored by AFGL, Liou and Stoffel[6] and Feddes and Liou[7] have reported on techniques to estimate the total mass of cirrus clouds and middle level clouds from infrared data. Estimates of integrated liquid water from microwave data have been reported by Staelin et al[8] and rainfall rates by Wilheit et al. [9] The estimates were made only over oceans since microwave emissivities are highly variable over land.

Although these techniques provide useful information for some cloud conditions, they are not presently suitable for a climatology of nose tip erosion. The microwave technique is a poor predictor of ice above the melting level of a rain cloud, but erosion is quite sensitive to ice particles at high altitudes. The infrared techniques developed by Liou[6,7] and others show promise for thin ice clouds and some layered situations but are of limited application for thick cloud systems.

These techniques are based on models of cloud radiation. However, aircraft observations of cloud particles in heavy weather situations hazardous to nosetips have found distributions of cloud particles which are extremely unlike distributions used in any cloud radiation models. The aircraft sensors have detected ice fragments, aggregates, graupel, rimed particles, dendrites, and other irregularly shaped particles. These uncertainties as to shape make it difficult to calculate phase functions for single scattering, leaving aside the enormous additional complications of multiple scattering. The aircraft have also observed great variability of cloud particle distributions in different volumes of the same cloud, which implies that a theoretical approach would have to guess at the particle size distribution of the cloud and consider major variations with altitude.

The difficulties in generalizing theoretical approaches to the full range of cloud conditions erosive to nose tips led us to review the literature on empirical approaches. We found numerous publications describing methods to infer cloud properties from satellites. Cloud properties which have been estimated from satellite data and which are related to the density profile of hydrometeors include cloud top

6. Liou, K-N, and Stoffel, T. (1976) Remote Sensing of Cirrus Cloud Compositions From Satellites, AFGL-TR-76-0027, 81 pp, University of Utah, Sale Lake City, Utah 84112.

7. Feddes, R. G., and Liou, K-N (1977) Cloud Composition Determination by Satellite Sensing Using the Nimbus VI High Resolution Infrared Sounder, AFGL-TR-77-0123, 140 pp, University of Utah, Salt Lake City, Utah 84412.

8. Staelin, D. H., Kunzi, K. F., Pettyjohn, R. L., Poon, R. K. L., and Wilcox, R. W. (1976) Remote sensing of atmospheric water vapor and liquid water with the Nimbus 5 microwave spectrometer, J. Appl. Meteor. 15:1204-1214.

9. Wilheit, T. T., Chang, A. T. C., Rao, M. S. V., Rodgers, E. B., and Theon, J. S. (1977) A satellite technique for quantitatively mapping rainfall rates over the oceans, J. Appl. Meteor. 16:551-560

altitude, cloud type, cloud thickness and rainfall. Satellite measurements of thermal radiation at 8 to 12 μ m are routinely used to estimate cloud altitude. The measured radiances are converted to the temperatures of a blackbody, weighted over the spectral interval of the sensor, and along with a temperature altitude relation, used to estimate cloud altitude. Colder temperatures correspond to higher clouds, while warmer temperatures correspond to lower clouds. The altitudes are often underestimated when satellites view cirriform clouds since theory and experiment have shown that cirriform clouds may be semitransparent to terrestrial radiation. Reflected sunlight and thermal radiation have been combined to infer cloud types by Booth[10] and by Shenk, Holub and Neff.[11] Clouds which are highly reflective and warm are low clouds such as stratus. Clouds which are poorly reflective and cold are thin high clouds such as cirrus. Clouds which are highly reflective and cold are thick clouds such as cumulonimbus or nimbostratus, which are expected to be the most erosive to reentry vehicle nosetips. Reflected sunlight has been related to cloud thickness by Reynolds and Vonder Haar,[12] Griffith and Woodley,[13] and Kaveney, Feddes, and Liou[14] and they conclude that the thickest clouds appear the brightest. Reflected sunlight and also thermal emission have been related to rainfall in a number of investigations. Martin and Scherer[15] have summarized work up to 1973. Griffith et al[16] have tested the concepts extensively using visible and infrared imagery from geosynchronous satellites. They have found that areas of active convection and rainfall in the tropics are brighter or colder on the satellite visible or infrared photographs than inactive regions.

In summary, other studies have shown that clouds which are highly reflective at visible frequencies and which appear rather cold at infrared window frequencies tend to be high, thick, and produce precipitation. Such clouds are also likely to be erosive to reentry vehicle nosetips, so that visible and infrared satellite data are expected to be useful for estimating erosion parameters.

1.5 Approach

The Satellite Correlation study used an empirical approach to relate satellite measurements to erosion parameters. Aircraft flights were made underneath satellites in a variety of cloud conditions. Non-linear equations were developed to relate infrared temperatures and visible luminances observed by satellite to erosion parameter estimates based on aircraft measurements of cloud and precipitation particles. Satellite data, aircraft data, and a case study are described in Section 2.

Studies were first directed toward techniques to estimate the altitudes and ice content of cirrus clouds. The studies were justified by early observations that cirrus clouds eroded the nosetips of high velocity reentry vehicles and by the fact

(Because of the large number of references cited above, they will not be listed here. See Reference Page 79, for References 10 through 16.)

13

that existing climatologies of cirrus cloud were quite limited. Aircraft and satellite measurements taken in 1974 demonstrated that cirrus altitude and ice content could be estimated to useful accuracies from multispectral infrared radiances measured by the NOAA Vertical Temperature Profile Radiometer (VTPR). However, by 1975, customer emphasis shifted from cirrus clouds to all clouds with particles larger than about 50 μm. For this more general problem, a combination of visible and infrared data from NOAA Scanning Radiometers (SR) were found to be more useful than VTPR data, because the VTPR technique was saturated by ice contents in excess of about 100 gm^{-2} integrated through a vertical column. Final VTPR studies were reported by Bunting.[17]

Preliminary correlations were developed between satellite visible and IR data and weather erosion as represented by the Environmental Severity Index (ESI), defined in Section 2.5. The correlations were applied to a sample month of data over Eurasia and maps showing areas exceeding certain threshold values were generated. A time lapse film showing daily distribution of ESI values greater or equal to two for one month over the area was also produced. A successful demonstration of this work in April 1976 was followed by a request for a full year of climatology over Eurasia, the Kwajalein and Wallops areas.

Since 1976, the preliminary correlation between ESI and satellite data was supplemented by more cases of satellite and aircraft measurements in heavy weather situations. Some cases of simultaneous satellite and radar measurements of clouds were also taken. Correlations were developed for erosion parameters other than the ESI. Calibrations were acquired for NOAA geostationary satellites so that the correlations based on polar orbiting satellites could be applied to geostationary satellites, which provide data over most of the Western Hemisphere at 30-min intervals. The calibrated geostationary satellite data were used in real-time to forecast conditions for erosion measurements at missile test ranges.

Further details of the observational programs, correlation studies, climatologies, real-time applications, verifications, and important computer programs follow.

2. OBSERVATIONS

2.1 Satellite Data

Data from the NOAA ITOS series of satellites were used to correlate erosion parameters and satellite observations. These correlations were then applied to a

---

17. Bunting, J.T. (1976) Cloud Properties from Satellite Infrared and Visible Measurements, AFGL-TR-76-0287, 6 pp.

14

year of NOAA archive to produce climatologies of certain erosion parameters. The NOAA Scanning Radiometer (SR) archive was the most suitable data base for several reasons. First, data were available every day starting in April 1973. Therefore, data were available for the last 10 months of the period February 1973 to January 1974, which had been selected by ABRES for intensive studies of weather over target areas. Second, the data were available for the entire Northern Hemisphere, which includes areas where calibration flights were made, test ranges, and target areas. Finally, the data were mapped, calibrated, and available on magnetic tape.

Data from the geosynchronous satellites GOES 1 located at 75° W and SMS 2 located at 135° W were used in real time to plan aircraft sounding flights in conjunction with passes of the polar-orbiting NOAA satellites, to produce real time aerial distributions of erosion parameters in the Wallops and Kwajalein test ranges, and to verify some of the established relationships.

2.1.1 ITOS SATELLITE DATA

Data which were correlated to aircraft measurements were from Scanning Radiometers (SR) aboard the polar orbiting NOAA ITOS 2, 3, 4, and 5 satellites. The one year climatology was from NOAA 2 (April 1973 to 19 March 1974) and from NOAA 3 (20 March to 31 March 1974).

Details of the NOAA SR archive have been described by Conlan.[18] The archive includes simultaneous IR and visible measurements once per day over the Northern Hemisphere. The satellites are sun-synchronous and pass over mid-latitudes at about 0900 to 1000 local time. The visible sensors respond to light at wavelengths 0.52 to 0.72 μm except for NOAA 5 whose range is about 0.44 to 0.92 μm. The IR sensor responds at 10.4 to 12.5 μm in the IR window region. Energy calibrations are applied to provide a data bank as homogeneous as possible. Variations in the spectral response of different visible or IR sensors are considered insignificant for our application. Both the visible and IR are archived in an 8-bit format. The visible code is proportional to luminance in foot-Lamberts. The maximum, or saturation value of 254 is approximately the luminance of a perfectly diffuse or Lambertian reflector at the top of the Earth's atmosphere when the sun is overhead. Throughout this study the visible data are retained in the 8-bit scale of 0 to 254. The coded IR values are converted to °K according to Table 1 for subsequent use. The archive of visible has been normalized for solar elevation by dividing each value by cosine θ where θ is the zenith angle of the sun. Observations in the IR array are much less sensitive to viewing geometry. The IR archive includes a small correction for limb darkening due to water vapor absorption. A daily quality control is used to monitor the visible and IR.

18. Conlan, E. F. (1973) Operational Products from ITOS Scanning Radiometer Data, NOAA Technical Memorandum NESS 52, 57 pp.

Table 1. Conversion of IR Coded Values to °K
for the NOAA Scanning Radiometer Archive

Coded Value	Temperature °K
0	164.0
1	165.0
.	.
.	.
.	.
78	242.0
79	242.5
80	243.0
81	243.5
.	.
.	.
254	330.0
255	Missing

Data from 12 or 13 consecutive orbits are archived in the form of 2048×2048 arrays for each hemisphere.[*] The array of visible and IR data is aligned with the conventional numerical weather prediction grid, so that the arrays are equally spaced on a polar stereographic projection as shown in Figure 1. The spacing of adjacent grid points on the surface of the Earth increases from about 6 km at the Equator to about 13 km at the poles as shown in Figure 2. The grid spacing is 1/32 of the spacing of the National Meteorological Center grid. Horizontal resolution of the original satellite data is roughly 3 km for the visible channel and about 6 km for the IR channel near the satellite subpoint. The grid is in some instances larger and in other instances smaller than the horizontal resolution of the original radiometer data, depending on whether the data are visible or IR, on the zenith angle of observation by the satellite and the latitude of the grid point. When the original radiometer data are of finer resolution than the array, for example, when the radiometers are looking straight down, no attempt is made to average values close to the array point—only the last value processed is retained.

---

[*]This archive was changed to 1024 × 1024 on 15 September 1976. At times of additional cloud truth observations after this date, satellite passes were specially processed for us on the original scale of 2048 × 2048 thus assuring the best possible data for correlation or verification purposes.
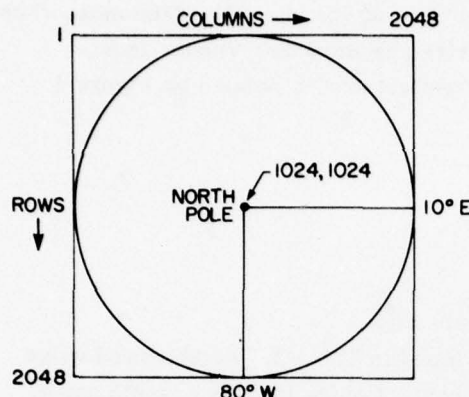
Figure 1. Satellite Archive Data Array Over the Northern Hemisphere
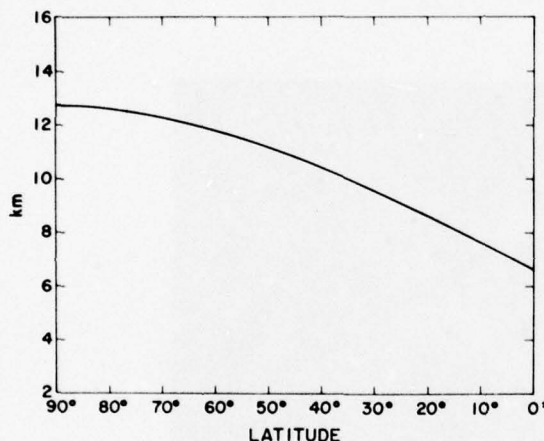
Figure 2. Satellite Archive Data Mesh Size vs Latitude

In spite of the normalization of the visible for the solar zenith angle, inconsistencies in brightness are often noted at the swath edges between satellite passes. These inconsistencies can be seen in Figure 3, an image generated from archived data. Where the satellite looks eastward toward the morning sun, forward scattering causes the cloud to appear excessively bright. Where the satellite looks westward, the weaker back scattering causes the same cloud to appear relatively dark. These irregularities were reduced using the bi-directional reflectance model of Sikula and Vonder Haar.[19] They developed correction factors from available summaries of cloud reflectivities observed by aircraft or satellites at different

19. Sikula, G. J., and Vonder Haar, T. H. (1972) Very Short Range Local Area Weather Forecasting Using Measurements from Geosynchronous Meteorological Satellites, Final Report for Contract F19628-71-C-0073, AFCRL-72-0260.

17

viewing angles and solar elevations. The original tables were expanded to include satellite zenith angle intervals of 60 to 70 and 70 to 80 for use with GOES data. The additional factors were based on data summarized by Raschke, Vonder Haar, Pasternak, and Bandeen.[20] The geometry of reflectance is defined by Figure 4 with

ζ the solar zenith angle,

ψ_1 the solar azimuth angle,

θ the satellite zenith angle,

ψ_2 the satellite azimuth angle,

ψ equal to $\psi_1 - \psi_2$ the relative azimuth angle.

From these angles correction factors can be found in Table 2. An observed value of visible luminance, or brightness, already corrected for the sun's zenith angle, is multiplied by the appropriate correction factor.
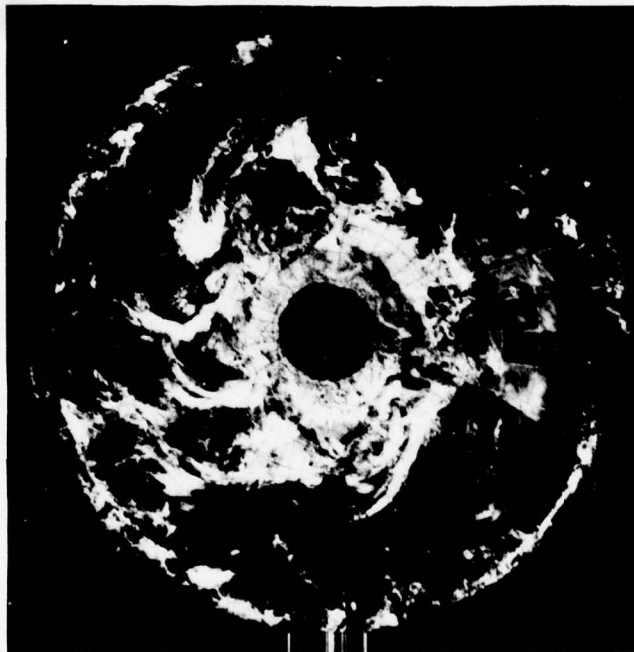
Figure 3. Visible Sensor Imagery Generated From the Digital Archive for 14 and 15 February 1975. Coast-lines do not appear in the archive

20. Raschke, E., Vonder Haar, T.H., Pasternak, M., and Bandeen, W.R. (1973) The Radiation Balance of the Earth-Atmosphere System from Nimbus 3 Radiation Measurements, NASA TN D-7249, 71 pp.

18
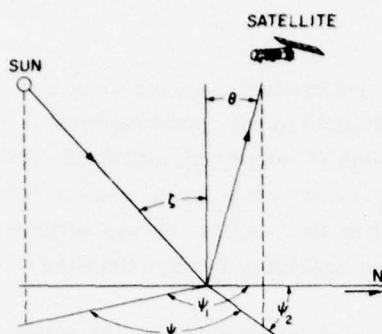
Figure 4. Geometry of Reflectance

Table 2. Correction Factors (χ/r) to Adjust Observed Brightness to Reflectance from an Isotropic Surface With the Sun Overhead

2-A	$0° \leq \zeta < 25°$	$\chi/r = 1.02 =$ constant
2-B	$25° \leq \zeta < 45°$ (Linear interpolation between Tables 2-A and 2-C)	
2-C	$45° \leq \zeta < 60°$	

θ \ ψ	0°-30°	30°-60°	60°-90°	90°-120°	120°-150°	150°-180
0°-10	1.00	1.00	1.00	1.00	1.00	1.00
10°-20°	0.93	0.93	0.93	0.95	0.95	0.95
20°-30°	0.90	0.90	0.93	0.93	0.93	0.90
30°-40°	0.87	0.87	0.90	0.93	0.88	0.83
40°-50°	0.83	0.83	0.85	0.85	0.80	0.70
50°-60°	0.75	0.75	0.76	0.76	0.68	0.53
60°-70°	0.73	0.73	0.81	0.77	0.62	0.50
70°-80°	0.70	0.72	0.80	0.75	0.56	0.39

2-D	$60° \leq \zeta < 80°$

θ \ ψ	0°-30°	30°-60°	60°-90°	90°-120°	120°-150°	150°-180°
0°-10°	1.04	1.04	1.02	1.00	1.00	1.00
10°-20°	1.07	1.04	1.00	1.00	0.98	0.98
20°-30°	1.04	1.04	1.00	0.97	0.93	0.93
30°-40°	0.97	0.97	0.97	0.93	0.86	0.80
40°-50°	0.84	0.87	0.92	0.86	0.74	0.70
50°-60°	0.72	0.78	0.82	0.75	0.64	0.60
60°-70°	0.68	0.78	0.83	0.74	0.50	0.41
70°-80°	0.62	0.74	0.79	0.68	0.39	0.28

In order to apply correction factors, the three bi-directional angles must be calculated. It was decided to do this for each 10 × 10 data array in the archive. This corresponds to a square of about 100 km on a side at temperate latitudes. This increment of resolution provides angles within a degree or two of being correct for all points in the SR array. Inspection of Table 2 shows that angular errors of this magnitude produce correction factor changes that are considered well within the overall accuracy of the table.

The hemisphere archives do not list which array points belong to a particular orbit; therefore, it is necessary to make this determination first. Then the three angles for the center of each 10 × 10 array can be calculated knowing the ephemeris data of the satellite and sun. An example of array determination by orbit for the Northern Hemisphere for 14 and 15 February 1975 is given in Figure 5. This pattern identifies the orbits of the composite image shown in Figure 3.

In Figure 5, orbit 1134 represents the earliest data in the array, while orbit 1146 represents the latest data, which is 12 orbits or 23 hr later. The pattern of orbits does not exactly exhibit circular symmetry, due to the method of entering the orbital data on the array. All of the data for a given orbit is written on the array when the orbit is processed; however, data from orbits processed later will replace the data processed earlier when a spatial overlap of orbits exists. When all of the data for a particular orbit is entered in the archive, the pattern looks like orbit 1146, which was in fact the last orbit processed so that its eastern side replaced some of the data for orbit 1145 while its western side replaced some of the data for orbit 1134. When orbits are processed in order, the pattern looks like orbits 1137 to 1145 on Figure 5. When orbits are processed out of order, the pattern looks like orbit 1135, which was written on the array at some later time than orbit 1136, and replaced some of the data on the eastern half of 1136. This reversal of orbit processing can occur when two orbits of data are stored on the satellite tape recorders and read out later.

The order in which orbits were processed was determined by looking at the pattern of discontinuities on images of the arrays. In general the pattern remains similar from day to day except for rotation around the pole and occasional variations near the dateline, at about 30° E.

The size of the satellite data array which was selected for comparison with cloud truth information was based on several factors. It was noted in the introduction that at the start of the study the satellite VTPR data were of principal interest. These data are for square areas of about 70 × 70 km at satellite nadir enlarging to rectangular areas about 70 × 108 km at left and right limits of the scan. Through most of the data gathering period, the size of the SR sample was made roughly the same as the size of the VTPR measurement over the area of interest for comparative purposes. This size area also proved to be representative

20

of the area sounded by aircraft. Ideally, cloud truth should apply to vertical columns throughout the cloud and be instantaneously determined at the precise time of the satellite scan. In practice, spiraling ascents or descents at 300 to 400 m min^{-1} and about 35 km in diameter proved to be the fastest flight pattern adequate for particle sampling.
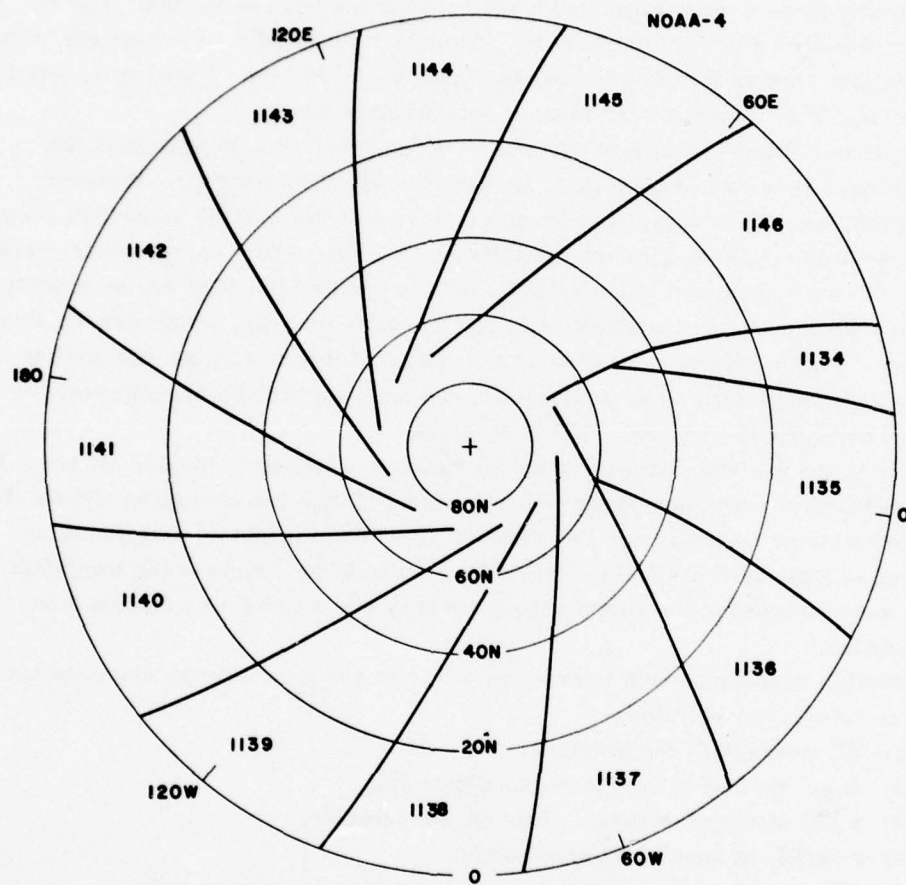
Figure 5. Pattern of Satellite Data by Orbits for the Northern Hemisphere 14 and 15 February 1975

The SR data are routinely placed into the NMC grid with care, nevertheless small position errors can usually be found. In order to minimize these errors, and place the data as closely as possible over the aircraft sounding, printouts of the SR

21

area of interest were made. Transparencies showing coast and latitude—longitude lines were prepared in the same scale as the printouts. These were generated from an archive of coastlines, rivers, lakes, and geopolitical boundaries referenced to latitude—longitude.[*] The SR printouts were then analyzed to determine the shifts necessary to fit the landmarks. In cases without landmarks near the area of interest, Very High Resolution Radiometer (VHRR) images obtained from NESS were hand gridded by anchoring the grid to visible landmarks. Positions of prominent cloud features were determined and transferred to the transparencies. The SR printout was then shifted to the best fit. Often both techniques were applied. The average grid shift to the SR data over locations in the eastern US was up 1, left 1 data point. The maximum shift found was three data points.

Neither of these techniques could be used for cases near Kwajalein in the Pacific Ocean because of the lack of landmarks and VHRR imagery. However, through the use of photographs at 16-min intervals of the WSR-57 radar PPI scope, small isolated echoes of showers could be pin-pointed. Their corresponding images could often be pin-pointed in the satellite data to position the SR array accurately. This approach requires the radar films to be timed correctly, which was not always the case. Furthermore, by checking the location of towers and the atoll outline during a period of anomalous propagation, it was found that the azimuth scale on the PPI photography required a -2° correction.

Due to the variable nature of tropical clouds and showers, sample SR areas had to be reduced to a few data points in some cases. In the extreme case, the satellite sample had to be reduced from the standard 70×70 km (about 50 data points at 35° N to as little as 7.5×7.5 km (one data point at 9° N). None of the Kwajalein cases were included in the correlations, but they are discussed in Section 5 on Verification.

Satellite variables which were extracted from the area through which the aircraft sampled were as follows:

(1) $\overline{IR}$, average IR temperature, °K,

(2) $H_{\overline{IR}}$, altitude in km corresponding to $\overline{IR}$,

(3) $\sigma \overline{IR}$, standard deviation of the IR temperature,

(4) $\sigma IR / \overline{IR}$, IR coefficient of variation,

(5) $\overline{B}_N$, average normalized visible brightness in arbitrary units,

(6) σB, standard deviation of brightness normalized only for sun zenith angle,

(7) $\sigma B / \overline{B}$, brightness coefficient of variation.

---

[*]The original archive was prepared by NESS; it was refined to one point every one-tenth of a degree for some areas by Cozzens.[21] The refined archive is now used by NESS for all gridded displays.

21. Cozzens, D.E. (1974) Technique to Earth Locate and Analyze Data from Satellite Sensors, pp 13-36, Burke, L. (1974) Met and Math. Anal. Final Rept. Regis College, AFCRL-TR-74-0558.

The above variables were entered in a stepwise multiple regression program to determine the best coefficients to predict erosion parameters as computed by simultaneous aircraft soundings. The results are discussed in Section 3 of this report.

2.1.2   GOES-1 and SMS-2   GEOSYNCHRONOUS SATELLITE DATA

Geosynchronous satellite data were not available to the Satellite Correlation study during the first series of flights in the winter of 1973 and 1974. Subsequently, our first use of the geosynchronous visible and IR imagery was for planning aircraft sounding flights. Sectorized pictures were received by C-5 telephone line from NESS. In the beginning these had to be gridded using our own library of grids along with NASA ephemeris predictions. Later the images were received already gridded. Their use helped greatly in forecasting sounding sites 4 to 6 hours in advance of aircraft flights. A more significant use of geosynchronous data was possible after the Man-computer Interactive Data Access System (McIDAS) became operational at AFGL since digital data could be obtained and processed. Once programs were perfected to navigate the data and convert it to NOAA satellite equivalents, it became possible to print out visible and IR data and erosion estimates over small specified areas in real-time.

General information on the geosynchronous satellites has been reported by Bristor[22] and is summarized here. Visible sensors respond in the 0.55 to 0.75 μm range while IR sensors respond in the 10.5 to 12.5 μm range. Their spectral response characteristics are reasonably close to those of the NOAA series of satellites thus facilitating the conversion process. Before reaching McIDAS the geosynchronous data are "stretched" so that the rate of data transmission is slower and adjustments are applied to the visible to make each scan line compatible with adjacent lines. The data stream is then returned to its respective satellite and re-transmitted. Information from GOES-1, located at 0°, 75° W, and SMS-2 over 0°, 135° W can be received, but not simultaneously, at AFGL.

In order to compare data from the polar-orbiting NOAA series of satellites with data from the geostationary satellites GOES-1 and SMS-2, available information on sensor calibration was reviewed. No conversion factors were necessary for IR data since all the satellites had IR sensors calibrated in °K. For visible data, ground calibrations established before launch were used to develop the following equations.

To convert 6-bit visible data from the geostationary satellites to the 8-bit NOAA satellite scale:

---

22.   Bristor, C. L. (1975) Central Processing and Analysis of Geostationary Satellite Data, NOAA Tech Mem. NESS 64, Washington, D.C., 155 pp.

$$C_N = \left(\frac{C_{G1}}{28.1}\right)^2 \times 55.6 , \tag{1}$$

$$C_N = \left(\frac{C_{S2}}{28.9}\right)^2 \times 55.6 , \tag{2}$$

where C_N is the 8-bit NOAA count,

C_{G1} is the 6-bit GOES-1 count, and

C_{S2} is the 6-bit SMS-2 count.

Brightness normalization for solar elevation is performed by McIDAS as follows:

$$B_N = \frac{C_N}{\cos \theta} , \tag{3}$$

where

$$\cos \theta = \sin \delta_C \times \sin \delta_S + \cos \delta_C \times \cos \delta_S \times \cos (\lambda_C - \lambda_S) , \tag{4}$$

with the symbols δ and λ referring to latitude and longitude, and the subscripts C and S referring to cloud and sun.

Corrections for bi-directional reflectance (Table 2) cannot be calculated presently within McIDAS due to limited storage capacity. These are currently calculated externally and then a single factor is inserted in McIDAS to produce fully normalized brightness for the area of interest.

Maximum resolution at the sub-point of the geostationary satellites is 8 km in the IR and 1 km in the visible; therefore, the visible should be combined to provide a value comparable to the smallest possible IR element. Within the 8 km IR element there are eight lines of visible each containing eight pixels. Present practice is to average all eight pixels out of one of the eight lines and to assign the value to the entire square. All eight lines cannot be averaged due to computer limitations. Actual sizes of one of these IR elements are, for example, over Wallops Island 9.8 km N-S × 6.2 km F-W (from GOES-1); and over Kwajalein 8.1 km N-S × 15.2 km E-W (from SMS-2).

The navigational accuracy of positions at sea level depends on how recently an orbital perturbation was introduced and how close the navigational landmarks are to the area of interest. For example when a rather distant landmark like Lake Titicaca in S. America is used to navigate in the central USA, an accuracy of 2 to 4 km can be attained after four pictures. After 8 to 10 pictures the accuracy improves to about 1 km.

24

It is important to remember that when zenith angles to the satellite are medium to large the position of high clouds is in considerable error. For example, at Kwajalein, where the zenith angle to SMS-2 is 65°, a cloud 10 km high will be navigated about 20 km west of its true position unless corrections are applied.

2.2 Aircraft Data

Aircraft flights in clouds viewed by satellites were made by four different aircraft from January 1974 to October 1976. A USAF C 130-A aircraft made 22 cloud soundings, while a C 130-E made 15, a Cessna Citation operated by MRI, Inc., made two and a Lear 36 operated by Aeromet, Inc. and MRI, Inc. made three. The C 130 aircraft and Citation were used until 2 March 1976 and the Lear jet was used after that date.

Aircraft flights were directed to suitable cloud conditions by a cloud forecast from AFGL. The forecast was primarily a 2- to 6-hr extrapolation of GOES IR pictures, hourly weather station reports and NWS facsimile products to the time of satellite pass. The forecasts were made necessary by time required to reserve airspace from the FAA and to fly to the area of interest. Early in the program flights were locked into the forecasted location. Later, however, the aircrews acquired some ability to make last-minute changes in the flight destination based on their own observations.

2.2.1 C-130 AIRCRAFT AND DATA REDUCTION

The C-130 aircraft were based at Langley AFB near Norfolk, Virginia; soundings were made as far as 1000 km inland from Langley but not over several hundred kilometers out to sea. Most sounding patterns were spiral descents around navigational beacons with entry into the highest clouds timed to coincide as best possible with the satellite pass. Since airspace suitable for rapid ascents and descents is difficult to find over the eastern U.S., it was often advantageous to plan flights in zones restricted to military flights. The C-130 aircraft ceiling is about 10 km; in a few cases cloud tops exceeded this level so top altitudes had to be estimated by the flight director.

Additional eye observations from the aircraft were:
    (a) The depth of cloud required to obscure the sun's disk,
    (b) Halo phenomena,
    (c) Ice particle form, size, and intensity as seen on the "snowstick" probe,
    (d) Presence of rime and its rate of formation,
    (e) Change of particle phase,
    (f) Cloud levels, types, fractional coverage, and
    (g) Estimates of cloud optical density.

Hydrometeor and atmospheric probes aboard the C-130's are listed in Figure 6 along with their depiction on the aircraft. Unfortunately data from the hydrometeor probes frequently had limited utility due to malfunction, lack of a full understanding of what the instrument sensed or difficulties in performing an analysis.

C-130E 40571
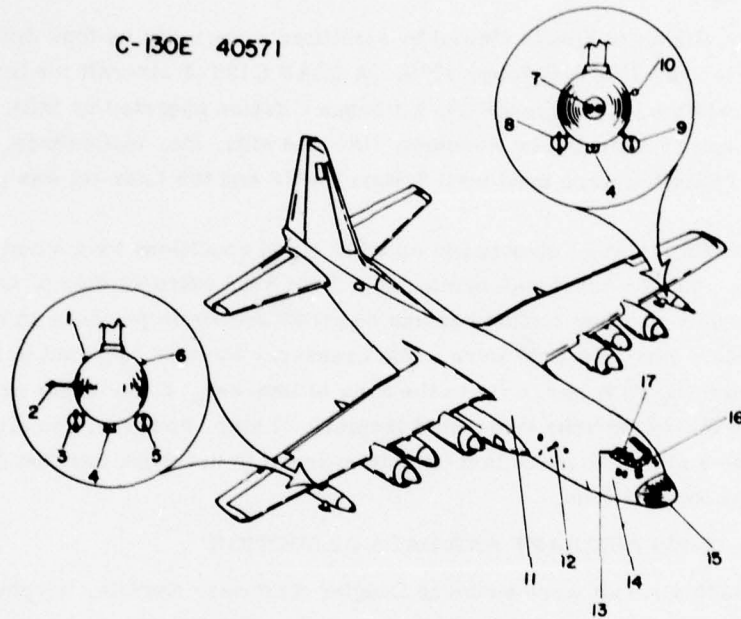
KEY:
1. DEW POINT HYGROMETER PROBE
2. PMS 1-D AXIAL SCATTER PROBE (2-30µ)
3. PMS 1-D PRECIP. PROBE (300-4500µ)
4. HYDROMETEOR FOIL SAMPLER
5. PMS 1-D CLOUD PROBE (20-300µ)
6. TOTAL AIR TEMPERATURE PROBE
7. EWER PROBE
8. PMS 2-D PRECIP. PROBE (200-6400µ)
9. PMS 2-D CLOUD PROBE (25-800µ)
10. JW CLOUD WATER PROBE
11. PDP-8/E COMPUTER & LINE PRINTER
12. FORMVAR HYDROMETEOR REPLICATOR
13. VISUAL HYDROMETEOR PROBE
14. I.N.S. & DOPPLER RADAR
15. AN/APQ-122 K_a & 5CM WEATHER RADAR
16. 16mm NOSE CAMERA
17. PROBE LIGHT

Figure 6. Atmospheric Probes Aboard the C-130E Aircraft

Analysis of the hydrometeor foil samples (Church, Pocs, and Spatola)[23] and the
formvar replicator were particularly difficult. On the other hand, LWC profiles of
useful accuracy could be constructed when the available data were coupled with the
excellent eye observations, surface observations of precipitation rate, and PPI
radar data.

When precipitation reached the ground, a rainfall rate over the sample area
was estimated from rain gauge and radar data. The precipitation rate was con-
verted to mass density using the logarithmic relationships for rain, small snow,
and large snow shown in Figure 7. These relationships were based on summaries
by Plank.[24] The estimated mass density for precipitation was simply extrapolated
upward to the generating altitudes of the clouds. The mass density estimated for
rain was increased to a consistent value for snow above the melting level.
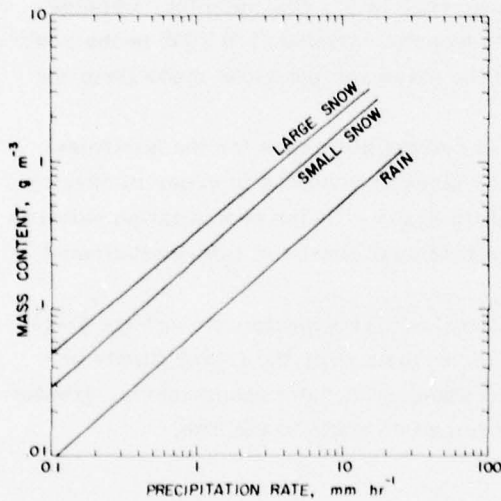
Figure 7. Precipitation Rate–Mass
Density Relationships for Rain,
Small Snow, and Large Snow

For each C-130 sounding, an altitude profile of hydrometeor density was con-
structed which was as consistent as possible with all the sources of data. Recent
measurements of ice mass vs temperature by the University of Washington and

23. Church, J. F., Lt Col, Pocs, K.K., and Spatola, A.A. (1975) The Continuous
    Aluminum-Foil Hydrometeor Sampler; Design, Operation, Data Analysis
    Procedures, and Operating Instructions, AFCRL-TR-75-0370, 70 pp.
24. Plank, V. G. (1974) Hydrometeor Parameters Determined from the Radar Data
    of the SAMS Rain Erosion Program, SAMS Rept. No. 2, AFCRL-TR-74-
    0249, 86 pp.

Meteorology Research Inc. which are given by Hobbs, Radke and Atkinson[25] and profiles through 16 storms at Wallops Island as shown by Berthel,[26] were used as basic guidance in constructing profiles of liquid and ice mass. The expertise of Dr. Robert M. Cunningham, Senior Scientist at AFGL, was drawn upon to finalize all profiles. An example of a sounding and the construction of a profile is given in Section 2.3.

2.2.2 LEAR 36 JET AIRCRAFT

The Lear jet ceiling is about 13.7 km; all flights in the USA topped the highest clouds. Its sounding pattern was a racetrack with a length of about 50 km along a radial from a navigational aid. Climbing soundings were usually made to prevent fogging of the PMS probes.

Details of the High Altitude Weather Aircraft Data System (HAWADS) are given by Booker and Windes.[27] Instrumentation is essentially the same as that aboard the C-130's except for the lack of the formvar replicator, foil sampler, Doppler radar, and EWER probe. In most cases the two-dimensional (2D) PMS probe could be used to classify particle type as input to the mass computations made from the one-dimensional (1D) data.

The greatest remaining difficulty was in making allowance for the horizontal motion of the hydrometeor system during the aircraft sounding in order to develop a LWC profile at the exact time of the satellite scans. Radar precipitation patterns showing echo velocities and trends were the principal source of information used to make these adjustments.

In general the Lear system benefitted from earlier experiences with the C-130 systems and the Lear soundings were an improvement over the C-130 flights because of improved instrumentation and understanding of the measurements, greater flexibility in site location and less time consumed en route to the site.

2.3 Radar Data

2.3.1 SPANDAR RADAR

The SPANDAR (Space Range Radar) is located at Wallops Island, Virginia. It is a high resolution (0.48° beam width) "S" band (10.7 cm wavelength) tracking radar having a peak power output of 3 MW. Minimum detectable mass for bullet-

25. Hobbs, P.V., Radke, L.B., and Atkinson, D.G. (1975) Airborne Measurements and Observations in Cirrus Clouds, AFCRL-TR-75-0249, Sci. Rept. No. 1, University of Washington, Seattle, Washington, 117 pp.

26. Berthel, R.O. (1975) A Climatology of Selected Storms for Wallops Island, Virginia, 1971-1975, SAMS Rept. No. 4, AFGL-TR-76-0118, 32 pp.

27. Booker, R.D., and Windes, J. (1977) HAWADS Equipment Description and Operational Manual, Aeromet, Inc., AFGL-TR-77-0066, 115 pp.

rosette particles is about 0.001 g m^{-3} at a distance of 50 km. The radar is calibrated by measuring echo returns directly over a disdrometer.

A program was initiated to gather data from this radar at times of NOAA satellite passes and later at times of GOES 1 satellite scans over the area. Radar scans were taken over a 34° azimuth sector. These data were to be processed to give integrated mass over squares corresponding to NOAA grid squares. The program for analysis of four cases, three of which contained detectable echoes, was not completed in time for this report.

Data from SPANDAR Range Height Indicator (RHI) scans can be processed by a Liquid Water Content Analyzer to estimate a mass profile with 250 m increments of height and also the ESI_p. Radar reflectivities are converted to mass estimates by means of logarithmic relationships based on radar to aircraft data comparisons for various particle-types and temperatures. These profiles are for a column about 250 m along the beam and of varying width across the beam. At a distance of 60 km the width is about 500 m. Sample volumes are therefore very small compared to samples by satellite, nevertheless, some comparisons of ESI_p derived by radar and satellite are discussed in Section 5, Verification.

2.3.2 TRADEX RADAR

The TRADEX (Target Resolution and Discrimination Experiment) radar is located on the Kwajalein Atoll in the Pacific Ocean. It is also an "S" band radar having a wavelength of 10.17 cm, 0.3° beam width and minimum detectable mass of 0.007 g m^{-3} for bullet-rosette particles at 50 km distance.

On one occasion RHI data were collected from this radar near the time of satellite scans, and a discussion of the analysis is given in Section 5, Verification.

2.4 Sample Case—8 October 1976

Each case used to develop the general relationships between satellite and erosion parameters became a small study in itself. All cases suffered from problems; timing differences between aircraft and satellite observations were inevitable and sometimes there were missing or conflicting measurements. This case illustrates good aircraft data, some timing difficulties and an unusual problem with the satellite data.

2.4.1 PRE-FLIGHT

During late afternoon of 7 October 1976 the Lear jet aircraft crew was alerted for a possible sounding flight from Hanscom AFB at Bedford, Massachusetts in the New York state or New England area on the following day at 1520Z (10:20 AM EST), the time of the NOAA-5 satellite pass. The National Environment Satellite Service in Suitland, Maryland, was notified that we might need the NOAA pass over that area.

29

At this time the NOAA archive had been reduced so it was necessary to request special processing of the pass.

On the morning of the 8th it was evident from the overnight sequence of geosynchronous satellite pictures that the thickest clouds, which were desired, were moving rapidly northeastward and out of the southern sections. It was therefore decided to go to Burlington, Vermont (BTV), near the Canadian border, only 30 min distant in flying time. The area was suitable for descent to low levels and hopefully would still be within the zone of thick clouds at pass time. An FAA clearance was obtained for an ascent and descent in a racetrack pattern 18 to 75 km out of BTV on the 180° radial. Plans were to fly from Hanscom AFB to Burlington, execute a missed approach to the field, then climb in the racetrack pattern to cloud tops. Breakout would be slightly ahead of pass time at 1521Z. Photographs of the top would be made, the aircraft would reenter the tops at pass time and descend in the racetrack pattern to 2 km, minimum safe altitude over the racetrack.

NESS was notified that we definitely wanted the NOAA pass processed in the old 2048 × 2048 element Northern Hemisphere format.

2.4.2   GENERAL SYNOPTIC SITUATION

Surface fronts and isobars are shown in Figure 8 superimposed on the digital visible NOAA-5 satellite data which was gridded and converted to an image by NESS through the use of an arbitrary gray scale. Also indicated on Figure 8 are the positions of Burlington (BTV), the weather radar station at Plattsburg (PBG), and Albany (ALB), the nearest RAOB station. The area of the racetrack sounding is indicated by arrows.

In the sounding area cool air flowing from the north was only 0.5 km deep; a transitional zone between cool and warm air was found between 0.5 and 1.7 km. Above this level winds were generally from the SW, averaging 72 km hr^{-1} at the 500 mb level. The tropopause, according to the 12Z ALB RAOB was at 12.7 km altitude. The PBG CPS-9 radar showed light echoes over the sounding area during ascent and before pass time, but no echoes at or after pass time. Echoes were moving from 220° at 88 km hr^{-1}. Figure 9, in which the ground pattern has been removed, shows echoes north and west of the racetrack at pass time. Aircraft sensors, however, detected very light rain until termination of the descent at 2 km and 29 min after pass time. The ceiling at BTV was 400 to 500 ft with light rain throughout the sounding period.

30
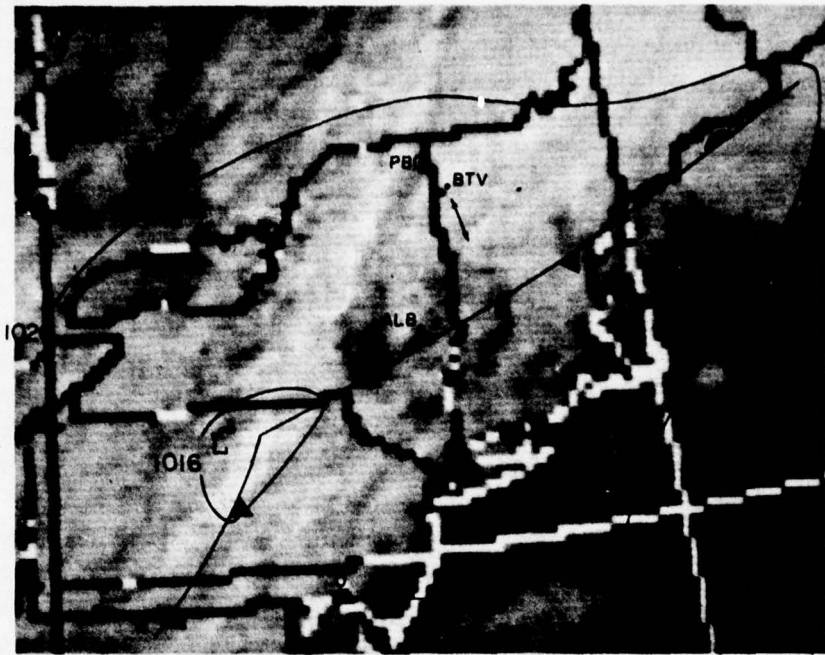
Figure 8. Display of NOAA-5 Digital Visible Data 1512Z
8 October 1976, Surface Synoptic Pattern at 1500Z and
Location of Reference Points
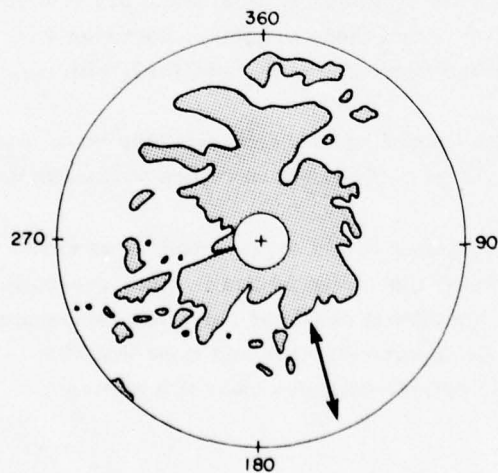
Figure 9. PPI Display of Weather
Echoes at Satellite Pass Time.
Outer range circle is 111 km. The
aircraft sounding took place along
the heavy arrowed line

31

2.4.3 HYDROMETEOR MASS PROFILES

Particle sizes and their numbers are measured primarily by Particle Measuring Systems (PMS) probes. These probes are optical array spectrometers which were developed by Knollenberg. Recent studies of their response to ice and snow particles can be found in Knollenberg.[28, 29] The one-dimensional (1-D) probes *count numbers in various ranges of length.* To reduce these data to mass it is necessary to classify the shapes of the particles counted and assign pre-determined conversion factors for each shape. Programs for converting these data to mass are described by Serbagi, Rodenheiser, and Kaplan;[30] Belsky, Kaplan, and Rodenheiser;[31] and Belsky, Francis, Kaplan, and O'Neil.[32]

The classification is greatly facilitated by data from the PMS two-dimensional (2-D) probes which can be processed to display particle shapes in two dimensions as shown in Figure 10.[*] In this display, time proceeds from left to right along each horizontal strip. Each particle that enters the field of view causes a vertical line whose length corresponds to 1.28 mm particle size. To the right of the line, the particle shape is displayed in the same scale. The time corresponding to one sample strip varies depending on the size and number density of particles. Not all particles are printed out in this display due to the huge numbers counted; however, ample data are available to detect changes in particle character. Figure 10 shows sample strips during ascent over the temperature range, +5°C to -40°C. Raindrops appear somewhat oval but should appear round. The elongation is caused by a slightly incorrect air speed in the processing program. Drop size at a temperature of +5°C was about 0.5 mm. At 0°C clumps of crystals were samples; one (circled) was about 2.5 mm across. As the temperature decreases particle size also decreases. At -10°C and -20°C dendritic crystals (circled) about 0.5 mm and 0.4 mm across were respectively sampled. From these printouts, particles encountered during the sounding were classified according to temperature, altitude, and time as shown in Table 3.

From the 1-D count data and eye classification of 2-D data, average mass was computed for 30 sec intervals or the equivalent of about 200 m layers in the atmosphere.

Mass density values were then plotted against height to give profiles as shown in Figure 11. These are for particles greater than about 50 μm in size, generally referred to as "precipitation" particles. Significant observer notes and temperatures are also shown. Mass profiles of liquid cloud particles assumed to be less than 50 μm in diameter and measured by the Johnson-Williams sensor are plotted separately as shown in Figure 12.

---

[*] Methods to eliminate the need for 1-D data by 2-D counting, sizing, and converting to mass estimates were under study at the time of this flight and could not be used.

(Because of the large number of references cited above, they will not be listed here. See Reference Page 79, for References 28 through 32.)

32
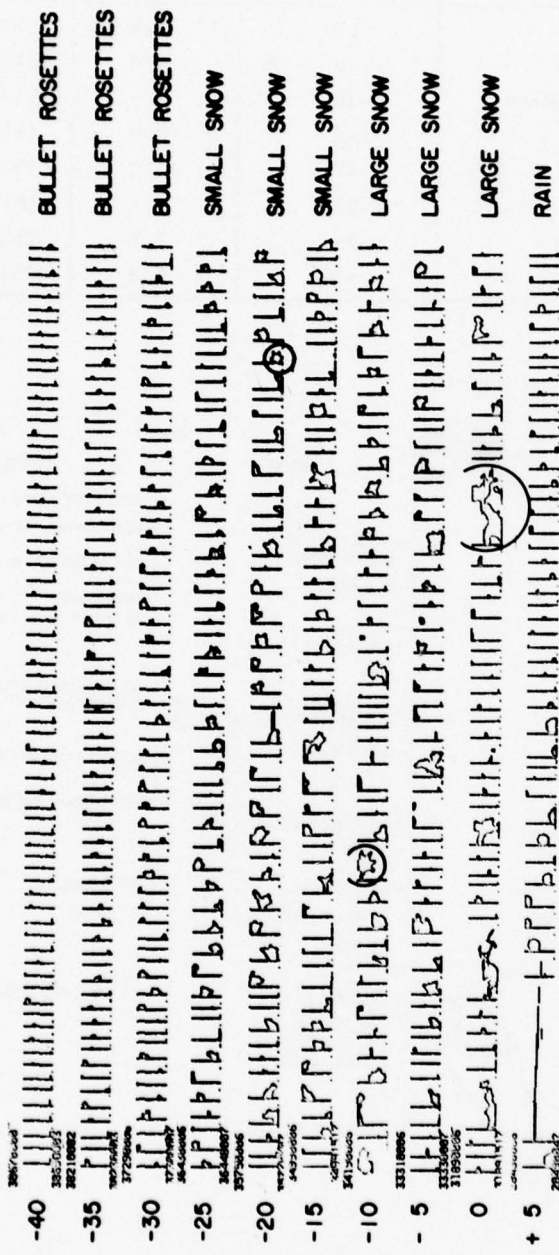
Figure 10. Particles Sampled by the 2-D-PMS Probe During Ascent 8 October 1976

33

Table 3. Particle Classification, 8 October 1976

Particle Classification Change	Temp. (°C)	Alt (km)	Time(Z)
Rain to large snow	+2	3.6	143746
Large snow to small snow	-10	5.6	144317
Small snow to bullet-rosettes	-26	7.9	144716
Bullet-rosettes to clear	-42	10.0	145100
Clear to bullet-rosettes	-45	10.2	152701
Bullet-rosettes to small snow	-29	8.4	153317
Small snow to large snow	-24	7.7	153447
Large snow to rain	+1	3.8	154517
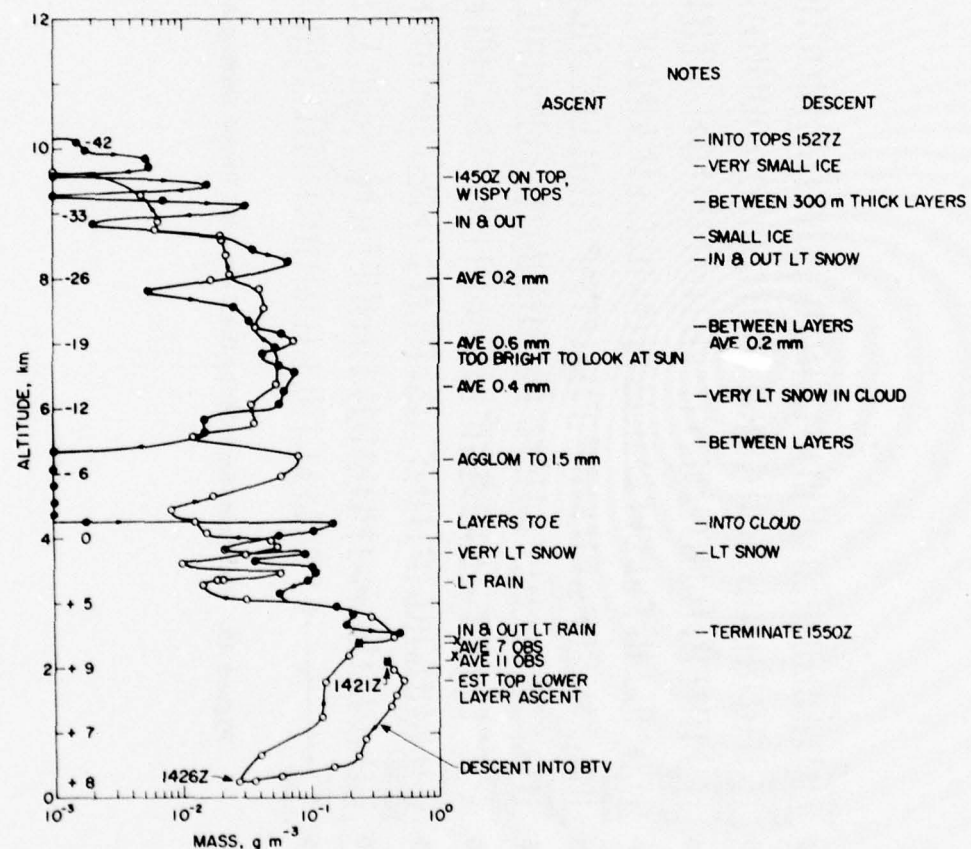
Figure 11. Vertical Profiles of Mass for Particles Greater than 50 μm in Diameter During Ascent and Descent 8 October 1976. Temperatures in °C are shown on the left with observer notes on the right. Points are PMS-1D system measurements. Points with crosses (X) are averages over more than one sampling run

34

ASCENT

DESCENT

ALTITUDE, km

DESCENT INTO BTV

MASS, g m^{-3}

10^{-3} 10^{-2} 10^{-1} 10^{0}
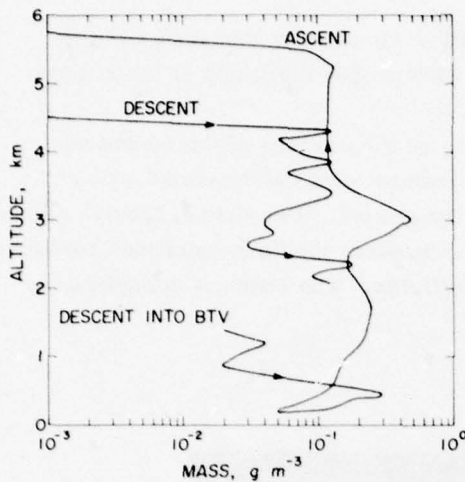
Figure 12. Vertical Profiles of Mass for Particles Less than 50 μm in Diameter Measured by the Johnson-Williams Sensor During Ascent and Descent 8 October 1976

The following chronological discussion of flight observations refers mainly to Figure 11 since erosion parameters are determined from the profile made up of precipitation particles. The first measurements were taken in a descent into BTV from 2.1 to 0.2 km during 1421 to 1426Z, almost one hour before pass time. The track was from about 18 km NW of BTV to BTV. Light to moderate rain was encountered. Ascent commenced over BTV at 142630Z over a ceiling of about 125 m. The aircraft immediately headed to the racetrack area south of BTV where it remained. During ascent the lowest clouds were topped at 1.8 km as noted by the observer but some cloud particles were measured up to 5.75 km as shown by Figure 12. The observer noted another liquid cloud layer which was topped at 3.3 km. Very light rain changed to very light snow at 3.6 km, about 250 m below the freezing level. A zone of agglomerates averaging 1.0 mm in size with maxima of 1.5 mm was noted at 5.2 km. This agrees well with a measured maxima of mass. Above 8.5 km the ice cloud was not solid and mass decreased significantly. Mass fell to less than 1 mg m^{-3} at 9.65 km and at 1451Z the aircraft broke through "wispy" tops at 10.0 km. These tops were therefore 2.7 km below the tropopause as measured near ALB. Character of the cloud tops is shown in Figure 13, a photograph taken at 9.96 km. The aircraft continued to climb to 12.96 km then it descended to reach the highest clouds at 1527Z, a few minutes after pass time. By this time the ice clouds were thinning; patches of liquid cloud could be seen through thin spots as shown in Figure 14. Between 5.35 and 4.5 km mass dropped below 1 mg m^{-3} indicating the injection of drier air (from the SW) and gradual weakening of the cloud system. A liquid cloud layer was entered at 4.5 km. The temperature was -2°C and rime built up rapidly. Ice crystals were found and they grew rapidly. Snow

35

changed to rain at 3.8 km and numerous layers of cloud were observed down to 2.1 km where the sounding terminated. The PMS probes fogged up at the 2.5 km level.

The profile at pass time was considered to be the average of the ascent and descent profiles. More specifically, average values were determined for 200 m layers centered at 0.1, 0.3 km, etc., above the ground. Two sets of tabular values are made, one for particles above about 50 μm in size, the "precipitation" particles, and one which includes the smaller "cloud" particles. The latter is considered to be the total mass or LWC.

Figure 13. Character of the Cloud Tops Observed from Top Level of 10.0 km During Ascent

36

Figure 14. Thinning Ice Clouds and a Patch of Liquid Cloud Photographed from 12.96 km at Start of Descent

2.4.4 SATELLITE DATA FOR 8 OCTOBER 1976

The visible satellite data were received and processed without incident. A visible image covering the area of interest was shown earlier in Figure 8. Digital data, normalized for the solar zenith angle, are shown in Figure 15. The aircraft racetrack sounding area is indicated. It was assumed that the cloud pattern remained unchanged while it moved at the velocity of the radar echoes during the sounding interval. Under this assumption the cloud area that corresponded to the sounding area is enclosed by the parallelogram shown in the figure. Ascent took place through the area enclosed above and to the right of the aircraft track and descent occurred through the area below and to the left of the track.[*] The IR data from this pass were inadvertently mapped near the Aleutian Islands. Transformation to the correct area involved more than rotation around the pole because of scale changes with latitude as shown earlier in Figure 2. The transformation was achieved by printing out a large area of visible and IR between two points of positive identification. The IR was then scaled to the visible and the correct area found. Coordinates of the IR are therefore different from the visible and when printed out, as in Figure 16, appear rotated approximately 90° to the visible.

[*]During the original analysis of this case a different echo velocity was used and therefore a different area was mapped in the digital data. Since the satellite parameters are only slightly changed, they have not been corrected and the regression analysis was not repeated.

37
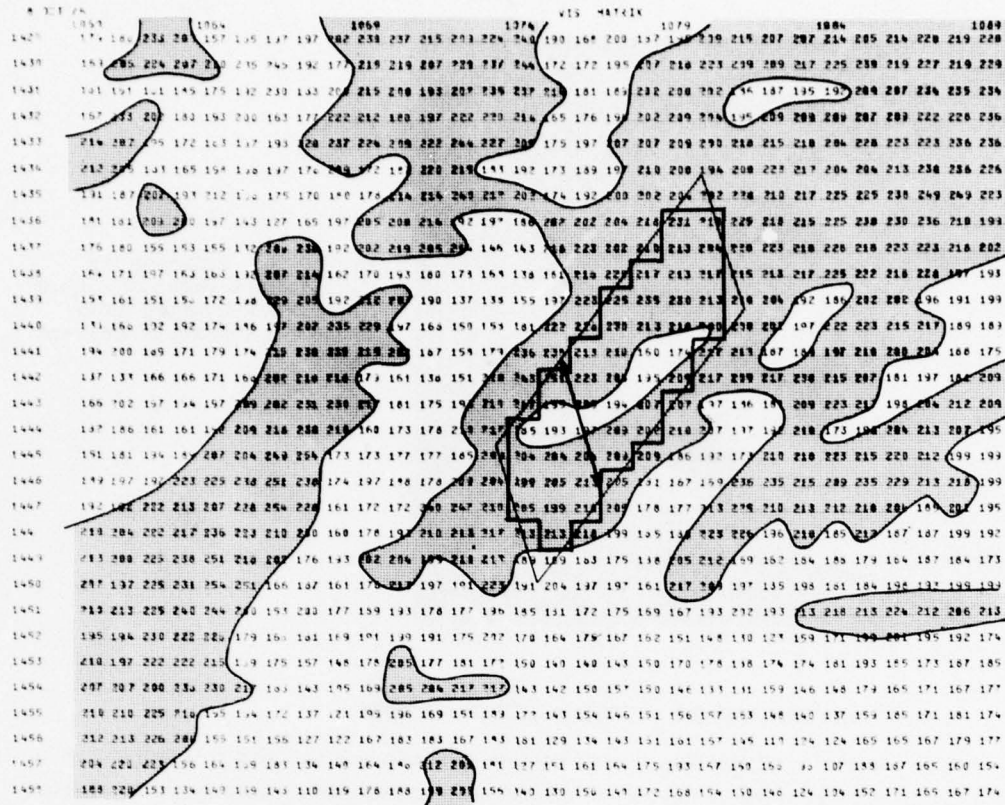
Figure 15. Aircraft Sounding Track and Area of Digital Visible Satellite
Data Assumed to Have Passed the Track During Ascent and Descent.
Areas brighter than 200 are stippled

The contour analysis in Figures 15 and 16 shows that relatively cold and bright
clouds were found over the ascent area and the northern end of the racetrack. This
pattern agrees with the rain pattern as seen by radar, aircraft observer notes and
decrease in mass from ascent to descent.

38
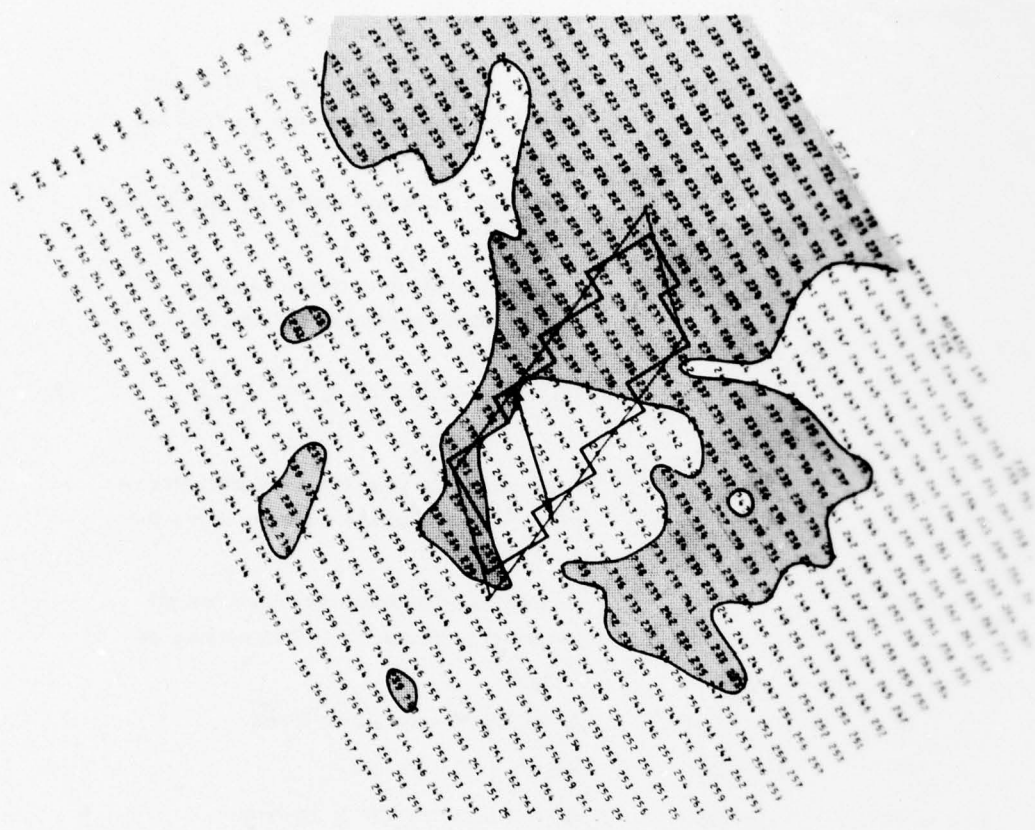
Figure 16. Same as Figure 15 Except for IR Data in °K. Areas colder than 240°K are stippled

2.5 Summary of Satellite and Erosion Parameters For All Cases

The satellite parameters which were determined for each case were described in Section 2.1.1. Individual values for each case are given in columns 1 through 7 of Table 4. Other variables listed in Table 4 were derived from aircraft measurements. They are:

Column No.

8	ΔH	The total thickness in km of all cloud layers having liquid or ice content of 1 mg m^{-3} or more.
9	LWC	Total liquid and ice mass for the column in g m^{-2}.
10	ESI$_p$	Environmental Severity Index for precipitation particles defined as

$$ESI_p = \int \rho\, HdH \ (g\ km^2\ m^{-3}) \quad\quad (5)$$

where ρ is the density of hydrometeors (g m^{-3}) and H is the altitude above the ground (km).

11	ESI$_T$	Environmental Severity Index for all particles, defined in the same way as ESI$_p$.
12	ADI	Accuracy Degradation Index.
13	ΔR	Range error in feet.
14	ΔS	Nose tip recession in inches.

Values of ADI, ΔR, and ΔS were calculated by TRW, Inc. The values for ΔR and ΔS are based on a TRW erosion model for a particular design of reentry system. The calculations use the altitude profile of precipitation mass density as input.

40

Table 4. Dependent Data Sample. Satellite parameters and corresponding integrated cloud mass, cloud thickness, and erosion parameters

No.	Date	$\overline{IR}$ °K	$H_{\overline{IR}}$ km	σIR °K	$\sigma IR/\overline{IR}$	$\overline{B}_N$	σB_N	$\sigma B/\overline{B}$	ΔH km	LWC g km^2	ESL_p g km^2 m^{-3}	ESL_T g km^2 m^{-3}	ADI	ΔR ft	ΔS in.
		1	2	3	4	5	6	7	8	9	10	11	12	13	14
1.	11 Jan 74	281.3	2.0	4.85	.0172	161.0	35.8	.1910	1.2	45.	.35	.36	.9	3.3	1.01
2.	14 Jan 74	259.0	4.1	4.07	.0157	91.0	25.2	.2880	.8	63.	.18	.22	.1	.2	.92
3.	1 Feb 74	263.9	3.2	7.49	.0284	57.0	21.4	.3680	.8	69.	.65	.65	1.6	5.2	1.08
4.	1 Mar 74	230.3	8.4	8.39	.0364	204.0	21.0	.0958	9.0	2035.	7.44	7.70	5.5	22.2	4.11
5.	3 Apr 74	281.7	1.7	4.71	.0167	40.0	13.3	.3230	0	0	0	0	0	0	.87
6.	8 Apr 74	229.8	8.5	3.48	.0151	203.0	17.2	.0849	8.4	661.	2.79	2.84	2.2	9.7	2.04
7.	24 Apr 74	265.3	3.2	3.96	.0149	184.0	30.0	.1660	1.0	56.	0	.08	0	0	.87
8.	28 Apr 74	247.5	6.5	10.29	.0416	203.0	22.0	.0975	8.6	731.	2.29	2.35	1.7	6.3	1.97
9.	2 May 74	234.2	8.6	6.74	.0288	176.0	17.7	.0832	2.8	325.	0.77	1.73	1.4	5.0	1.12
10.	15 Jan 74	283.7	1.3	1.80	.0063	137.0	18.0	.1250	.8	25.	0	.03	0	0	.87
11.	12 Jan 75	223.0	10.4	5.50	.0239	211.1	19.2	.0882	8.8	1067.	3.65	4.29	3.3	11.9	2.53
12.	14 Jan 75	261.1	4.0	4.50	.0172	112.8	44.0	.3000	2.6	486.	.16	.72	0	0	.97
13.	20 Jan 75	217.2	10.4	5.60	.0258	204.8	19.8	.0928	10.4	1082.	4.38	4.54	4.4	17.7	2.93
14.	22 Jan 75	248.4	6.6	6.70	.0270	141.2	28.4	.2110	5.6	178.	1.09	1.09	1.5	6.5	1.35
15.	23 Jan 75	248.6	7.0	4.80	.0193	97.8	20.9	.1710	3.4	71.	.59	.59	1.3	5.9	1.16
16.	25 Jan 75	248.0	7.2	5.60	.0226	157.9	36.3	.1910	8.6	474.	2.24	2.58	3.4	14.3	1.81
17.	27 Jan 75	262.9	1.2	3.20	.0122	123.1	29.7	.2200	1.6	60.	.01	.09	0	0	.88
18.	29 Jan 75	257.9	5.1	5.60	.0217	191.4	39.6	.2010	4.6	752.	.23	1.70	0	.1	.97
19.	4 Feb 75	251.1	6.8	3.30	.0131	175.2	19.9	.1100	8.6	736.	2.16	2.60	1.8	6.7	1.89
20.	11 Feb 75	256.5	4.1	4.10	.0160	128.2	36.4	.2360	4.0	33.	.07	.07	0	0	.91
21.	13 Feb 75	259.9	.9	4.20	.0162	102.3	16.7	.1140	1.4	11.	.01	.01	0	0	.27
22.	14 Feb 75	245.1	6.1	10.20	.0416	73.4	15.2	.1190	2.6	27.	.24	.24	.6	3.7	1.09
23.	23 Feb 75	235.8	8.5	9.70	.0411	192.5	35.0	.1750	7.0	362.	.74	1.45	1.4	5.7	1.16
24.	1 Mar 75	252.5	2.4	3.10	.0123	171.5	20.3	.1210	3.4	336.	.45	.67	.1	.2	1.06
25.	3 Mar 75	266.9	1.3	4.00	.0150	126.6	23.4	.3700	1.6	141.	0	.26	0	0	.87
26.	16 Mar 75	223.7	10.0	4.80	.0215	182.0	10.2	.0493	6.6	595.	3.20	3.20	3.7	14.8	2.20
27.	20 Mar 75	249.0	6.5	16.50	.0663	189.4	21.7	.0985	2.6	140.	.06	.16	.1	.7	.92
28.	26 Mar 75	266.0	1.5	6.40	.0241	104.5	48.3	.4060	.8	31.	0	.04	0	0	.87
29.	27 Mar 75	229.5	8.7	6.80	.0296	192.1	16.8	.0752	10.0	1314.	5.53	5.56	5.4	22.3	3.38
30.	4 Apr 75	247.6	5.6	4.60	.0186	167.0	18.0	.0927	5.6	370.	.64	.76	.1	.5	1.15
31.	10 Apr 75	261.1	4.4	3.40	.0130	168.5	15.8	.0825	5.0	751.	1.26	2.16	.4	.9	1.38
32.	22 Apr 75	259.7	4.2	4.90	.0189	135.0	18.8	.1295	3.6	41.	.04	.14	.1	.4	.87
33.	23 Apr 75	230.5	9.2	9.80	.0425	200.1	27.0	.1282	9.2	1967	7.30	7.78	6.1	25.4	3.99
34.	29 Apr 75	260.9	5.4	10.20	.0391	145.2	26.2	.1640	5.2	129.	.05	.59	.1	2.8	1.28
35.	30 May 75	244.1	8.0	8.20	.0336	220.1	18.5	.0841	10.4	817.	2.69	3.43	2.7	11.1	2.10
36.	1 Jun 75	248.7	7.9	7.00	.0281	162.4	27.1	.1500	3.4	255.	.98	1.32	1.5	5.1	1.15
37.	5 Jun 75	271.7	3.4	3.50	.0129	169.5	34.1	.2010	3.6	131.	.04	.32	.1	3.2	1.27
38.	11 Jan 76	241.5	6.8	4.80	.0199	175.2	36.6	.2010	7.4	1042.	2.64	2.64	1.3	4.4	2.17
39.	2 Mar 76	239.6	7.4	7.40	.0309	155.7	17.1	.0714	10.4	1127.	3.57	3.57	1.4	5.6	2.10
40.	21 Apr 76	233.7	8.8	4.80	.0206	180.7	31.3	.1560	10.2	880.	6.25	6.27	11.3	42.6	3.40
41.	8 Oct 76	241.4	8.6	6.50	.0417	155.7	18.6	.0896	10.0	1532.	2.88	4.27	1.9	8.0	2.25
42.	9 Oct 76	212.6	12.0	3.20	.0153	206.2	9.9	.0466	12.5	4938.	22.20	22.23	28.4	160.7	9.33

3. RELATIONSHIPS BETWEEN SATELLITE PARAMETERS AND EROSION PARAMETERS, LIQUID WATER CONTENT AND CLOUD THICKNESS

3.1 Transformation of Satellite Data to a Linear Form

Relationships between the satellite data and simultaneous aircraft estimates of erosion, LWC, and cloud thickness quantities were calculated by means of a step-wise multiple regression program. Since this program assumes linear relation-ships, and since it was obvious that satellite observed brightnesses and tempera-tures were not linearly related to erosion parameters, the brightness and tempera-tures were "linearized", that is, transformed into numbers which are linearly related to erosion parameters. It was also noted that the standard deviations and coefficients of variation of the brightness or IR temperature were not significant predictors of erosion parameters; therefore, only the averages of brightness, IR temperature and IR height were subsequently linearized and used.

Equations of the following forms were tested to develop the best linearization:

$$Y = A + B/X , \tag{6}$$

$$Y = 1/(A + BX) , \tag{7}$$

$$Y = A (X)^B , \tag{8}$$

$$Y = A + B/(C - X) . \tag{9}$$

In general, the hyperbolic form of Eq. (9) gave the best fit and the fraction, $1/(C-X)$, was used to linearize X.

As an illustration, the equation found to linearize brightness $\overline{B}_N$ to ESI_p, is:

$$ESI_p = -2.554 + 506.253 / (288.7 - \overline{B}_N) . \tag{10}$$

Equation (10) and the data points from which it was derived are shown in Figure 17. The correlation coefficient is 0.62 and the standard error of estimate is 1.61. In this case, the fraction, $1/(288.7 - \overline{B}_N)$, is used to linearize $\overline{B}_N$ before entry into the multiple linear regression program. The program then derives constants for multiple regression.

42
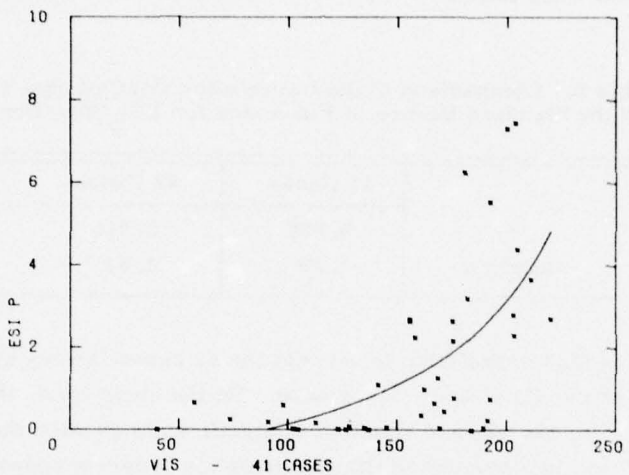
Figure 17. Data Points and Hyperbolic Equation Used to Relate Visible Data to ESI_p

3.2 Dependent Sample Size

Equations relating satellite parameters to erosion parameters were first developed from 38 cases with simultaneous aircraft and satellite measurements of clouds. Due to pressure for early results, the equations were applied to 3 months of satellite data over Europe and Asia. However, four additional cases having very good aircraft data became available later, so it was decided to include these as part of the dependent sample. This necessitated recomputations of the relationships and using the new relationships to replace the original output which had been delivered. For this reason, throughout the remainder of the report, reference will be made to equations based on data samples of different size, namely 38, 41, and 42 cases.

The most desirable prediction equations are usually found by using the highest possible number of cases in the dependent sample; however, in the present sample the last case, number 42, was extraordinarily high in water content and erosion parameters. For example, when ESI_p is considered, its value according to Table 4 is 22.20 as compared to the next highest value of 7.44. For a sample including this extreme case, the regression program will tend to fit an equation to the outlying point, at the expense of lower values, in order to obtain the best overall fit. More specifically, when regression analysis is applied first to 41 cases excluding

43

the highest case and then to all 42 cases the following correlations and standard errors of estimate were found.

Table 5. Comparison of the Correlation Coefficients (r) and the Standard Errors of Estimates for ESI_p Equations

	41 Cases	42 Cases
r	0.785	0.915
std error	1.20	1.51

At first glance the high correlation found with the 42 cases is very attractive and the residual error for the 42nd case is near zero. On the other hand, the standard error of estimate for the 42 case equation is significantly greater than that for the 41 case equation and is a serious limitation since the program sponsors specified that maximum accuracy was desired in the 2 to 8 range of ESI_p. Similar differences between the 41 and 42 case equations were found for all the predictands which led to the adoption of the 41 case sample for final regression analysis.

3.3 Erosion Liquid Water Content and Cloud Thickness Predictions From Brightness and IR Data

The regression equation used to predict ESI_p from brightness and IR data, based on the 38 case dependent sample is:

$$ESI_p = \frac{516}{\overline{IR} - 159.3} + \frac{149}{271.4 - \overline{B}_N} - 5.84 . \tag{11}$$

The correlation coefficient is 0.79 and the standard error of estimate is 1.20. Similar equations, which were developed to predict all the erosion parameters, LWC and cloud thickness based on the 41 case dependent sample, are shown in Table 6.

A plot of the 41 case equation for certain values of ESI_p is shown in Figure 18. Aircraft observed ESI_p values are also plotted to indicate the degree of scatter and ranges of visible and IR covered in the dependent sample. A dashed line shows the approximate range of satellite data from a large independent sample in May over Eurasia, and this range is not much greater than the range of aircraft cases.

Table 6. Equations, Correlation Coefficients, and Standard Errors of Estimate for Prediction of Erosion Parameters, LWC, and Cloud Thickness Based on 41 Cases

Equation	Correlation Coefficient	Standard Error of Estimate
$ESI_p = \dfrac{746.249}{(\overline{IR} - 148.800)} + \dfrac{177.500}{(288.700 - \overline{B}_N)} - 7.395$	0.785	1.265
$ESI_p = \dfrac{76.981}{(18.163 - H_{\overline{IR}})} - 4.932$	0.746	1.359
$ADI = \dfrac{810.318}{(\overline{IR} - 150.400)} + \dfrac{81.354}{(297.600 - \overline{B}_N)} - 7.317$	0.690	1.634
$ADI = \dfrac{71.371}{(17.581 - H_{\overline{IR}})} - 4.767$	0.698	1.615
$\Delta R = \dfrac{3138.756}{(\overline{IR} - 150.800)} + \dfrac{343.004}{(297.900 - \overline{B}_N)} - 28.409$	0.694	6.327
$\Delta R = \dfrac{312.715}{(18.162 - H_{\overline{IR}})} - 19.985$	0.704	6.238
$\Delta S = \dfrac{284.322}{(\overline{IR} - 153.500)} + \dfrac{83.710}{(288.900 - \overline{B}_N)} - 2.110$	0.774	0.560
$\Delta S = \dfrac{34.571}{(18.360 - H_{\overline{IR}})} - 1.287$	0.741	0.594
$LWC = \dfrac{476826.657}{(\overline{IR} - 71.460)} + \dfrac{110445.603}{(315.680 - \overline{B}_N)} - 2913.734$	0.734	362.011
$ESI_T = \dfrac{1065.209}{(\overline{IR} - 129.000)} + \dfrac{266.467}{(297.400 - \overline{B}_N)} - 9.058$	0.793	1.287
$\Delta H = \dfrac{209460.983}{(\overline{IR} - 1097.000)} + \dfrac{1200.841}{(355.100 - \overline{B}_N)} - 156.606$	0.830	1.894

Figure 18 like all the erosion equations, shows rapid increase in ESI_p as brightness approaches its maximum and as IR temperature approaches minimum values. It is of interest to note the behavior of the ESI_p curves for 273°, the melting temperature of ice. Precipitation cases with cloud top temperatures above 273°K will have few or no ice particles so that high ESI_p is not expected in mid-latitudes except during the infrequent cases of warm rain. The curves show that zero ESI_p is found with a brightness of 160 and that at the maximum brightness found within the data sample, namely 240, the ESI_p is 2. Extrapolation to brightnesses beyond the dependent data range is reasonable since very bright clouds just above freezing may represent warm rain in the tropics with significant ESI_p values.

45
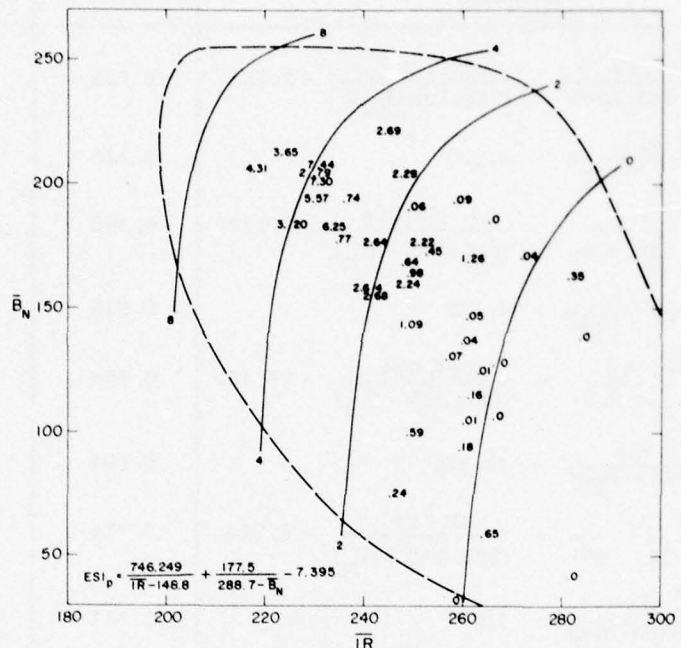
Figure 18. Plot of Equation Used to Predict ESI_p from $\bar{B}_N$ and $\overline{IR}$, Based on 41 Cases. Dependent data are shown

3.4 Erosion, Liquid Water Content, and Cloud Thickness Predictions From IR Data Alone

For the 6-month period, November through April, the visible brightness over Eurasia may be partly a measure of the reflection from snow cover, or, in mid-winter, it may be unavailable over northern portions due to darkness. These limitations forced us to consider special approaches for winter conditions. First, a brief experiment was run to determine the feasibility of using brightness for at least part of the 6-month period. Minimum reflection values were determined for 6-day running periods. These values were assumed to represent ground reflectance and were subtracted from the daily observations. As a result, more reasonable erosion values were calculated over clear areas but the effect of decreasing the brightness of heavy clouds yielded ESI_p values that were low. It was also found that over the frozen sea or tundra snow cover alone was often brighter than snow cover plus thin cloud, an observation not understood but possibly related to the reflective properties

46

of snow at low sun angles. In view of these complications, it was decided not to use the brightness in any form over Eurasia during the 6-month period.

Additional calculations revealed that the use of IR temperature or IR height ($H_{\overline{IR}}$) alone gave erosion predictions of almost the same accuracy as the use of both IR and brightness in the 41 case dependent sample. This sample was from a relatively homogeneous area over winter and spring where temperature-height profiles did not vary appreciably. However, in view of the much greater variation of temperature-height profiles over Eurasia during the 6-month period, the use of $H_{\overline{IR}}$ appeared to be more desirable than IR temperature alone. Therefore, $\overline{B}_N$ plus $\overline{IR}$ predictors were used for the months of May to October 1973, while the $H_{\overline{IR}}$ predictor was used for the months of April, November, December 1973, and January to March 1974. Equations using $H_{\overline{IR}}$ alone to predict all the erosion parameters, LWC, and cloud thickness from the 41 case dependent sample are given in Table 6. $\overline{IR}$ temperatures were converted to $H_{\overline{IR}}$ by means of average monthly temperature-height profiles. These profiles were developed by Spiegler and Fowler[33] from a 4 to 5 year data bank. A profile was made for every 32 original satellite grid points (the NMC grid). In practice each 5×5 data box used the nearest profile which was never more than 22.6 original grid points distant. At latitude 65° this is about 271 km. Larger errors in the converted $H_{\overline{IR}}$ value are likely to occur due to a day's departure from the average. Examination of standard deviations at standard pressure levels as given by Crutcher and Meserve[34] by month and area show a maximum of about 4° in April at 700 mb (3 km) over central Eurasia. In the Moscow area the maximum is about 3° at 700 mb (3 km) and at 500 mb (5.5 km), also in the spring months. These temperature variations are equivalent to about 0.7 and 0.5 km respectively, and when placed in the erosion equations give the range of uncertainty listed in Table 7.

Table 7. Erosion Parameter Uncertainties Corresponding to Maximum Monthly Standard Deviations of Temperature at Two Altitudes

	at 3.0 km	at 5.5 km
ESI_p	± 0.1	± 0.2
ADI	± 0.2	± 0.3
R	± 1.0	± 1.0
S	± 0.1	± 0.1

33. Spiegler, D. B., and Fowler, M. G. (1972) Four Dimensional World Wide Atmospheric Models (surface-25 km altitude) NASA CR-2082, Environmental Res. and Tech., Inc., Concord, Massachusetts 01742, 65 pp.

34. Crutcher, H. L., and Meserve, J. M. (1970) Selected Level Heights, Temperature and Dew Points for the Northern Hemisphere, NAVAIR 50-IC-52.

It is therefore concluded that use of average monthly temperature-height profiles introduces relatively small errors while saving significant time and expense.

Determination of heights above the ground from the 0 to 15 km profiles were made according to the following rules:

    (1) First, determine tropopause height.

        (a) If change of slope $\Delta H / \Delta T$ becomes ≥ 0.25 km $^\circ K^{-1}$ from 1 km level to the next going upward, this level is assigned the tropopause height.

        (b) If not, then level of lowest temperature is designated as the tropopause.

    (2) Height of IR temperature is then determined progressing downward from the tropopause level.

        (a) If IR temperature exceeds any in profile, assign to level of highest temperature in profile.

        (b) If IR temperature is lower than any in profile, assign to level of of lowest temperature.

Further tests revealed a bias when erosion parameters were calculated over a wide range of conditions from both the $\bar{B}_N$ plus $\overline{IR}$ and from the $H_{\overline{IR}}$ alone equations given in Table 6. The $H_{\overline{IR}}$ alone equations gave higher ESI_p in heavy weather. Therefore, in order to make the estimates over winter and summer as homogeneous as possible, erosion parameters were calculated from both $\bar{B}_N$ and $\overline{IR}$ and from $H_{\overline{IR}}$ alone for a large sample and compared. The sample was chosen to contain a minimum of zero erosion values. A comparison of the two equations was made for each erosion parameter over a critical range of values for that parameter. In comparing ESI_p from the two equations for example, cases with ESI_p between 0 and 8 according to the $\bar{B}_N$ plus $\overline{IR}$ equation were used. This reduced the sample size somewhat. The comparison consisted of developing a new linear regression equation between the two sets of ESI_p values from which an intercept and slope could be obtained.

The equations for converting erosion parameters derived from $H_{\overline{IR}}$ only to $\overline{IR}$ and $\bar{B}_N$ equations are listed in Table 8. Cases outside the limits given were excluded. Correlations, standard errors of estimate, and numbers of cases in the sample are also listed. In all cases, the erosion parameters from the $H_{\overline{IR}}$ variable alone must be reduced for best agreement with the $\bar{B}_N$ and $\overline{IR}$ equations. The most probable cause is overemphasis to cirrus cases in the $H_{\overline{IR}}$ only estimates. $\overline{IR}$ and $\bar{B}_N$ histograms over large areas show numerous cold but medium bright cases of cirrus which probably are underrepresented in the 41 case sample used to form the original equations. The equations in Table 6 were combined with those in Table 8 to provide the final equations which are shown in Table 9. A plot of final ESI_p equation for $H_{\overline{IR}}$ alone is shown in Figure 19. The figure shows that ESI_p values

48

of zero occur for systems having $H_{\overline{IR}}$ values up to 2.6 km. In the area of lowest mid-winter Eurasian tropopause heights, where maximum $H_{\overline{IR}}$ is about 8 km, the ESI_p will not exceed 1.8. Southern tropopause heights of 15 km will give an ESI_p of about 12.5 assuming that dense clouds are measured at that level.

Table 8. Conversions from Equations using $H_{\overline{IR}}$ Only to Equivalent Equations of $\overline{IR}$ and $\bar{B}_N$

Equation	Upper Limit	Correlation Coefficient	Standard Error of Estimate	Number[*] of Cases
$\widehat{ESI_p}_{\overline{IR}+\bar{B}_N} = 0.679(ESI_p)_{H_{\overline{IR}}} + 0.045$	8.0	0.892	0.582	26,850
$\widehat{ADI}_{\overline{IR}+\bar{B}_N} = 0.600(ADI)_{H_{\overline{IR}}} + 0.105$	11.0	0.895	0.584	26,885
$\widehat{\Delta R}_{\overline{IR}+\bar{B}_N} = 0.640(\Delta R)_{H_{\overline{IR}}} + 0.300$	50.0	0.907	2.189	26,885
$\widehat{\Delta S}_{\overline{IR}+\bar{B}_N} = 0.920(\Delta S)_{H_{\overline{IR}}} - 0.274$	4.0	0.893	0.355	26,816

[*]For 7 and 8 May 1973   Total data points   = 27,626

Satellite data missing = 741

Satellite data O.K. = 26,885

Table 9. Final Equations to Predict Erosion Parameters from $H_{\overline{IR}}$ Alone, Based on 41 Cases

$$ESI_p = \frac{52.270}{(18.163 - H_{\overline{IR}})} - 3.304$$

$$ADI = \frac{42.823}{(17.581 - H_{\overline{IR}})} - 2.755$$

$$\Delta R = \frac{200.138}{(18.162 - H_{\overline{IR}})} - 12.490$$

$$\Delta S = \frac{31.805}{(18.360 - H_{\overline{IR}})} - 1.458$$

49

$$ESIp = \frac{52.270}{18.163 - H_{\overline{IR}}} - 3.304$$
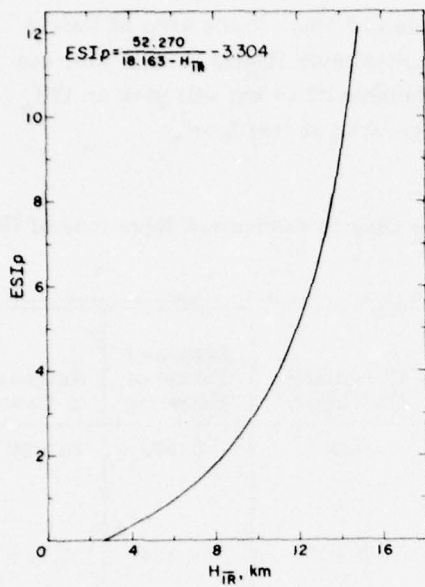
Figure 19. Plot of Final Equation Used to Predict ESI_p from $H_{\overline{IR}}$. Based on 41 cases

3.5 Probability Predictions

A probability model by Gringorten[5] was applied to the data in Figure 18 in order to establish the probabilities that a threshold of ESI_p would be exceeded as a function of cloud temperature, $\overline{IR}$, and brightness, $\overline{B}_N$. Figure 20 has the results for an ESI_p threshold of 5. Probabilities, based on the 38 case sample, are as high as 90 percent for the coldest and brightest clouds observed.

PROBABILITY ESI PRECIP ≳ 5
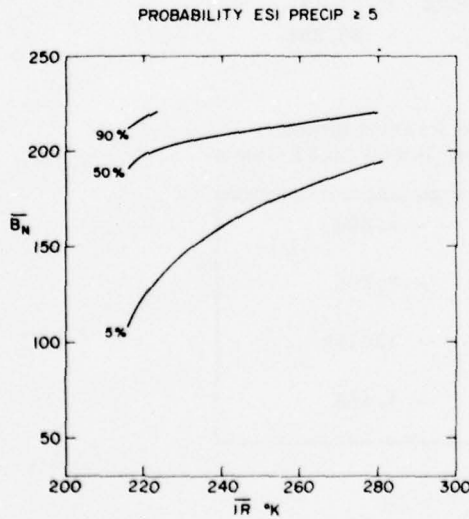
Figure 20. Probabilities of Exceeding an ESI_p of 5 Related to Satellite Measurements

50

4. APPLICATION—CLIMATOLOGICAL AND REAL TIME EROSION PARAMETERS

4.1 Program Schedule

In response to a letter from SAMSO, dated 7 May 1976, in which various climatologies of erosion parameters were requested, the program schedule in Table 10 was drawn up and approved by 23 June 1976.

Table 10. Program Schedule for Satellite Estimates of Erosion Parameters

|	Task	Date Due	Date Mailed
1.	Method Verification (as developed)	1 July 1976 to 1 October 1977	
2.	ESI_p maps		
	May to October 1973 (6 mos)	15 December 1976	10 December 1976
	April 1973, November to December 1973 (remaining 6 mos)		
	January to March 1974	1 October 1977	Cancelled
3.	Target statistics		
	May, July, October 1973 (3 mos)	1 October 1976	18 October 1976
	Remainder (9 mos)	1 October 1977	13 December 1976* 30 October 1977
4.	ESI_p - test areas		
	Wallops & Kwajalein		
	May to October 1973 (6 mos)	1 October 1976	10 October 1976
	Remainder (6 mos)	1 March 1977	8 March 1977
5.	ADI, ΔR, ΔS correlations		
	Test	1 March 1977	Verbal ok 21 April 1977
	Remainder (12 mos)	1 October 1977	3 October 1977

*3 mos only

Over the work period changes occurred, new products were generated and some of the original products requested were simplified but in general the program remained intact. Completion dates for the various parts of the program are also shown in Table 10.

4.2 Grid Size

Most of the dependent cases from which the regression equations were developed used satellite data averaged over 50 to 70 samples usually in parallelogram shaped areas. These are roughly equal in size to square areas of 8×8 data points. It was

51

decided that useful applications of the erosion equations could be obtained from
5 × 5 square areas, although the significance of equations when applied to smaller
areas was unknown at the time. Therefore, unless otherwise noted, all erosion
parameters derived from the NOAA satellite archive are for 5 × 5 squares which
range in actual size from 33 × 33 km at the equator to 61 × 61 km at 70°N. Further-
more, it was arbitrarily decided that a valid 5 × 5 computation required data from
at least 15 of the 25 possible data points.

4.3 Environmental Severity Index-Precipitation (ESI_p) Maps

ESI_p maps and target statistics are described in a separate annex to this re-
port. The annex is available to qualified agencies upon request to AFGL/LY,
Hanscom AFB, MA 01731.

4.4 ESI_p for the Kwajalein and Wallops Test Ranges

ESI_p values over 5 × 5 grid areas were computed from the 38 case $\overline{B}_N$ plus $\overline{IR}$
equation. Brightness was used year around, even at Wallops, since the prime areas
of interest lay over the sea. Arrays of values were printed out, one day per page,
and grid overlays were supplied for positioning the data.

A sample printout for the Wallops area with superimposed overlay is shown in
Figure 21. The geographical grid is skewed in relation to the satellite grid as
discussed in Section 2.1.1. Missing data are indicated by 999. A similar printout,
Figure 22, shows ESI_p for the Kwajalein area.

In the Wallops area, satellite data were frequently missing because a satellite
readout station is located at that site and interrupts local data when reading out
stored orbits. A count of useful ESI_p arrays at both test ranges is given in Table 11.

4.5 Realtime Application of ESI_p Erosion Parameter

Once it became possible at AFGL to accurately navigate data from the geo-
synchronous satellites, a program was written to normalize the brightness and
compute ESI_p in realtime. All grid data were for the nominal 8 km subpoint reso-
lution discussed in Section 2.1.2.

An 8 × 8 array of ESI_p values could be presented on the McIDAS CRT screen
3 min after the satellite scanned the clouds. A 50 × 50 array could be printed out
and positioned under a grid in 12 to 13 minutes.
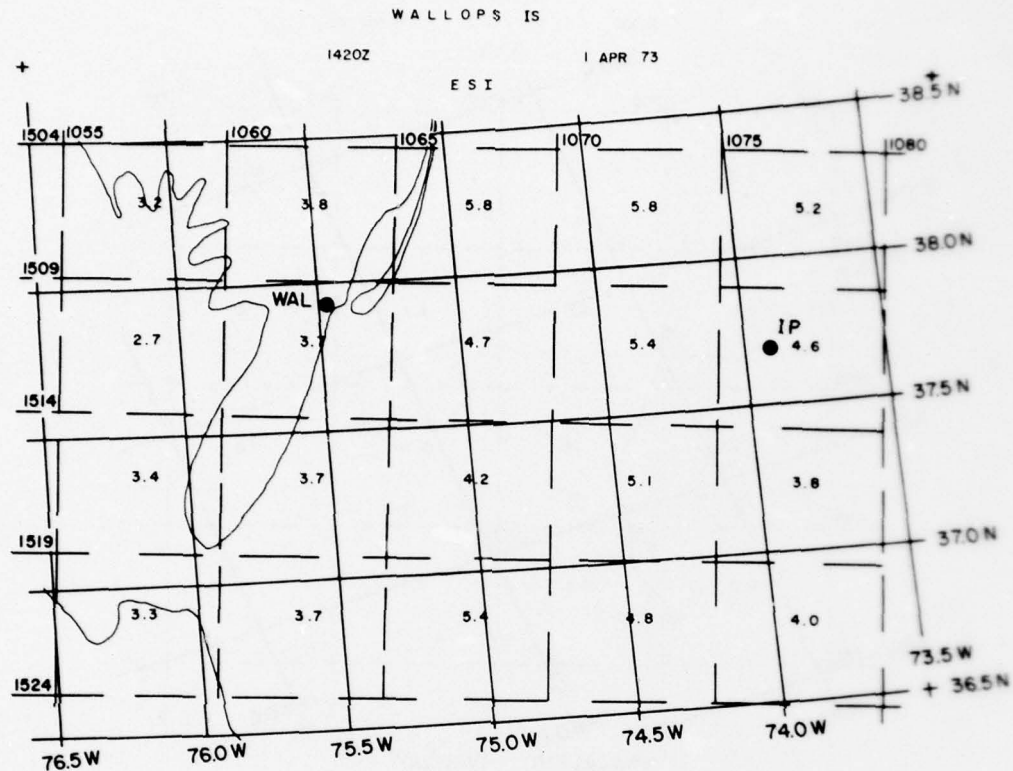
Figure 21. ESI$_p$ in the Vicinity of Wallops Island 1 April 1973, from the NOAA-2 Satellite

The ESI$_p$ data and cloud motions were frequently relayed by phone to the AFGL Weather Team at Wallops in the spring of 1977. Generally, positions were given in terms of azimuth and distance from Wallops. The ESI$_p$ estimates were used to approximate erosion in areas beyond reach of the SPANDAR radar. In addition, for the first time, comparisons of ESI$_p$ values obtained by radar and satellite become available in areas closer to the SPANDAR. Unfortunately, only a few quantitative comparisons were obtained but the team did become accustomed to the advantages and limitations of the satellite estimates.
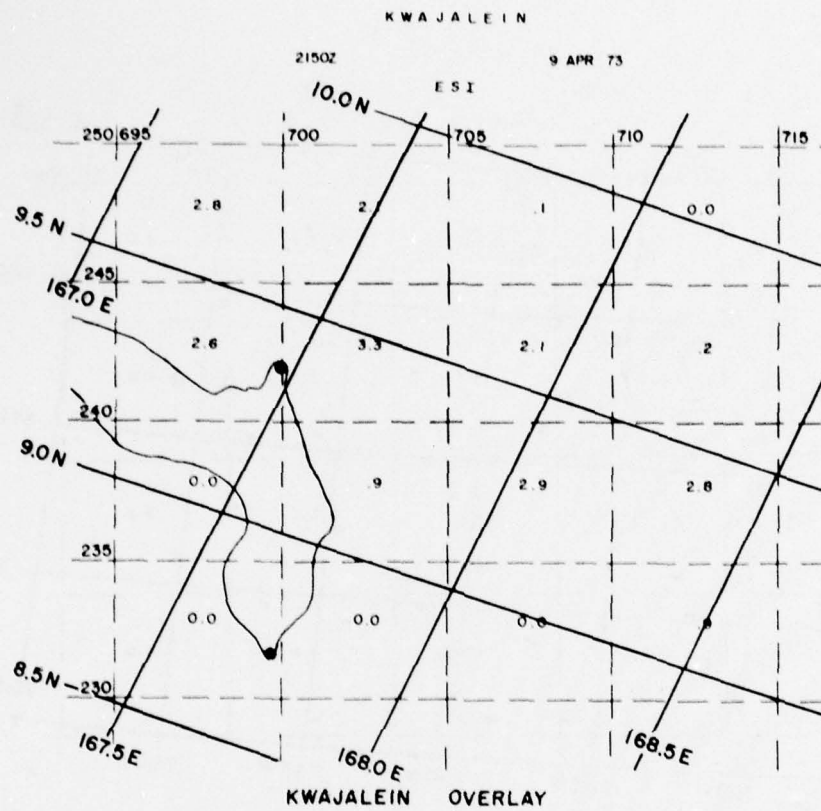
Figure 22. ESI_p in the Vicinity of Kwajalein Atoll 9 April 1973 from the NOAA-2 Satellite

Geosynchronous satellite estimates of ESI_p over and upwind of the Kwajalein area were first thought to be useless due to a zenith angle of 65° to the nearest satellite at 0°N, 135°W. However, ESI_p values were calculated from the eastern satellite for a small area which duplicated the viewing and sun angles to Kwajalein from the western satellite at the time of maximum interest. These were compared with values calculated 15 min earlier for the same area from the western satellite which looked down at only 12° from the vertical. The ESI_p values were surprisingly close, with maximum values in individual clouds differing by only a few percent. Naturally, the scales were different and narrow E-W variations in the clouds were not evident when viewed at the high zenith angle. Examples are presented in Section 5.5 of this report. After this comparison a procedure for relaying ESI_p patterns and cloud motions for realtime use at Kwajalein began.

54

Table 11. Frequency of Satellite Coverage at Test Ranges
During One Year

			Wallops Days With Data	Kwajalein Days With Data
April	1973		18	28
May	1973		19	31
June	1973		25	29
July	1973		24	29
August	1973		22	31
September	1973		24	29
October	1973		26	30
November	1973		24	25
December	1973		22	30
January	1974		23	30
February	1974		25	27
March	1974		16	26
		Total	268	345
		% Possible	73	95

Since the western geosynchronous satellite does not oscillate appreciably from the
equator in its orbit, it is possible to use master grids in equatorial areas. McIDAS
programs calculate latitudes and longitudes of the center and corner points of arrays
of satellite data. These indices are then used for positioning the overlay grids. The
most useful data were relayed near 2030Z or about 11 hr before the usual launch
window time. Data for upwind areas beyond radar range proved useful. Once
again comparisons between radar and satellite derived ESI_p were obtained within
radar ranges. A program of taping the data during the eastern night was developed
to facilitate subsequent analysis and comparisons. A sample printout of ESI_p values
and grid overlay is shown in Figure 23.

55
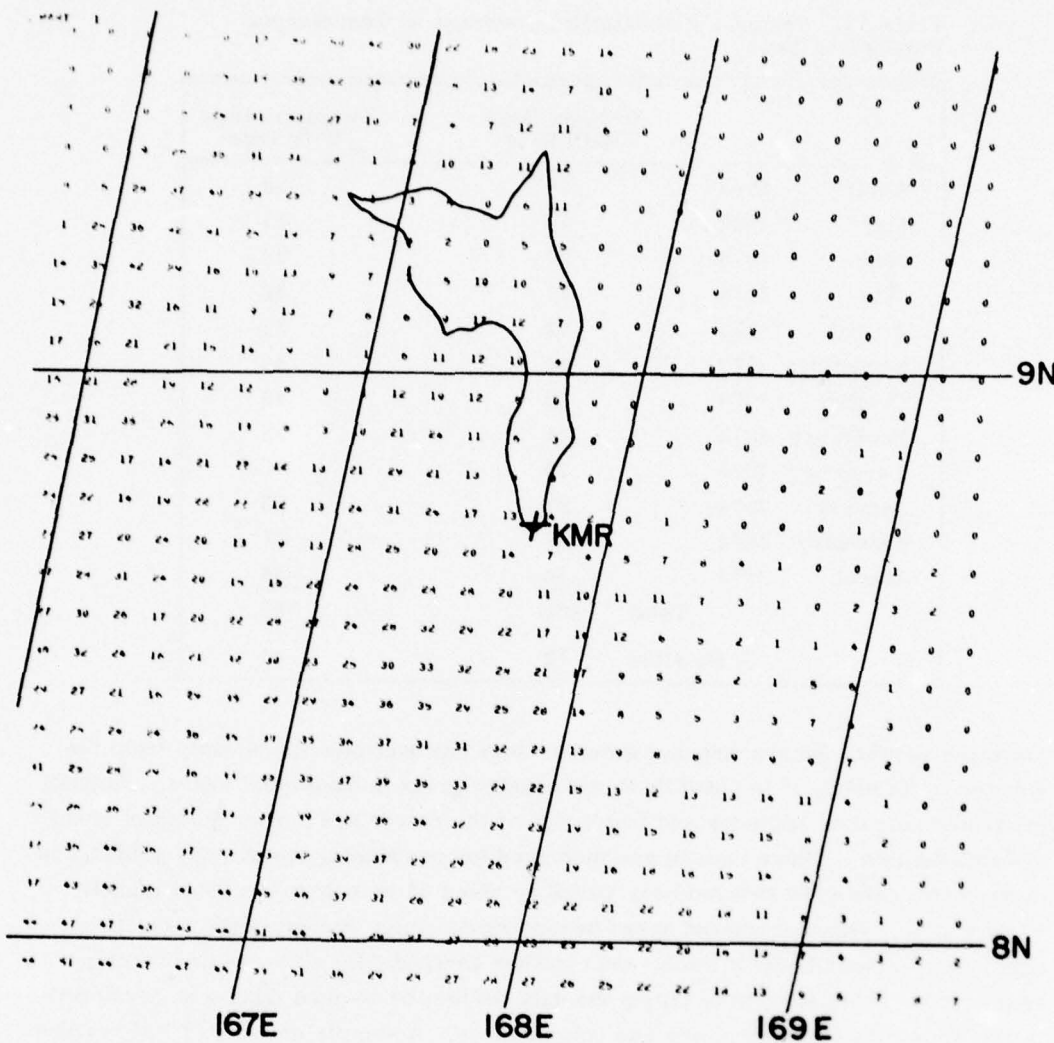
Figure 23. ESL$_R$ (in tenths) in the Vicinity of Kwajalein Atoll 21 July 1977 from the GOES-West Satellite

5. VERIFICATION AND INTERCOMPARISON

5.1 General

Five approaches were taken to verify estimates of erosion parameters from satellites and to intercompare them with estimates from non-satellite sources. First, the 41-case sample of satellite and aircraft estimates of erosion were examined

statistically by dividing the sample into two parts. This approach allowed equations to be checked against independent data and predicts how well the equations will work when applied to other sets of independent data such as the satellite data over target areas. Second, satellite estimates were compared with a limited sample of ESI_p estimates from radar at temperate and tropical latitudes. This approach is unique in that the radar ESI_p estimates are instantaneous and synchronous with the satellite. However, individual samples were for horizontal areas whose size was considerably less than the areas viewed by the satellite sensors. Third, satellite estimates were compared with a limited sample of ESI_p estimates from aircraft soundings from convective systems near Kwajalein. In this case, the technique for obtaining the mass profile from aircraft was the same as in the 41-case sample, but the comparisons yield useful information on the value of ESI_p estimates in highly convective areas which were not included in the 41-case sample. Fourth, another comparison shows the effects of slant viewing from a satellite on ESI_p values near Kwajalein. Fifth, a large sample of satellite estimates were compared with near synchronous ESI_p estimates from the AFGL II model at 11 stations in Europe and Asia. This comparison gives no information on the absolute accuracy of either method. It merely compares two different techniques for estimating ESI_p.

There are limitations to verifications which are important to remember. The most important limitation is that no accepted standard exists for measuring hydrometeor distributions over substantial volumes. The satellite correlation study has used procedures developed very recently by AFGL to support reentry system erosion tests and this technology is still undergoing refinement. Consequently, the extent of uncertainty in the hydrometeor measurements described is not well known. Another limitation is the fact that the satellite measurements of clouds have not been compared directly to measurements of nosecone erosion in clouds but rather to parameterized hydrometeor profiles (ESI_p, ADI) or calculated erosion effects (ΔS, ΔR). How the uncertainties in modelling erosion interact with uncertainties in satellite and aircraft measurements is not known.

5.2 Statistical Approach

A common approach in verification of empirical relationships is to divide available data into two mutually exclusive sets named the dependent set and the independent set. A relationship is developed from the dependent set and then applied to the independent set as a test. The errors generated in the test predict the expected accuracy in future use of the relationship with new sets of data.

A slight departure from this approach was necessary due to the limited number of dedicated and expensive aircraft flights available to our study. Only 41 cases were available when final applications had to be made. It was decided that the highest payoff would result by using all the cases to derive relationships rather than divide

57

the data and risk insignificant relationships. Applications proceeded with rela-
tionships based on 41 cases as discussed in Section 3.

A later experiment, however, revealed that similar relationships could be
derived from fewer cases so that the 41 case sample could be divided and relation-
ships could be checked. One of the 41 cases having a very low ESI_p was selected
at random and removed to give an even number of cases. The cases were then
ranked in terms of aircraft ESI_p and subdivided into 4 groups of 10 each so that
prediction errors from high and low ESI_p cases could be studied separately. The
Root Mean Square (rms) residuals in Table 12 in the column marked "dependent"
are the results when the 38-case ESI_p equation is used on the 40-case sample. [*]
The residuals are simply the differences between the aircraft observations of ESI_p
and the predictions of ESI_p from the equation. The residuals increase as ESI_p
increases; however, the quotient of the residual divided by the ESI_p decreases as
ESI_p increases. In the important range of ESI_p from 2 to 8, residuals are less
than the observed ESI_p. The residuals for ADI, ΔS, and ΔR exhibited similar
tendencies.

Table 12.   Root-Mean-Square (rms) Residuals of ESI_p in
Dependent (40 case sample) and Independent (2 $\times$ 20 case
samples)

Ranked Samples	Range of Aircraft ESI_p	rms Residuals	
		Dependent	Independent
Nos. 1 to 10	0.0 to 0.06	0.64	0.85
Nos. 11 to 20	0.07 to 0.65	0.66	0.76
Nos. 21 to 30	0.74 to 2.64	1.04	1.24
Nos. 31 to 40	2.68 to 7.44	2.24	3.66
Nos. 1 to 40	0.0 to 7.44	1.32	2.01

The residuals in Table 12 column marked "independent" are results when the
40-case sample is randomly divided in half, a prediction equation derived for each
half separately and then used to predict ESI values for cases in the other half-
sample. The independent residuals are higher than the dependent residuals, as
expected; however, since they are not appreciably higher and since all the predic-
tion equations are similar we expect that the extensive applications reviewed in

---

[*]The 38-case equation is reasonably close to a best fit to the 40-case sample since
the residuals of the last two cases from the predictions of the 38-case equation are
not large. Consequently, no special equation was derived for the 40-case sample.

58

Section 4 have errors which do not exceed the independent residuals given in Table 12. The results of Table 12 further imply that meaningful relationships could have been developed from a sample of cases half the size of the one available to this study.

5.3   Radar vs Satellite ESI_p Values

5.3.1   SPANDAR RADAR vs GOES-EAST SATELLITE— 24 FEBRUARY 1977

RHI data from the SPANDAR radar at Wallops Island were collected from 19 to 23Z. Scans not more than 3 min from satellite time were then processed to give ESI_p values at varying distances between 24 and 96 km from the radar. Levels of particle types and their transition zones were assigned by Dr. R. M. Cunningham at the time. These were based on air temperature and aircraft observation of the particles. Equations to convert radar reflectivities to mass densities for various particle types have been summarized by Plank. [24] During the first part of the period, echoes were found between about 3 and 9 km altitude with radar ESI_p of 0.1 to 2.2. Near the middle of the period, precipitation reached the ground and a maximum ESI_p of 12.4 by radar was computed. Shortly before the trend to higher ESI_p daylight waned and the comparisons had to be restricted to satellite ESI_p by $H_{\overline{IR}}$ alone.

The comparison is summarized in Table 13. The column marked "n" refers to number of samples. During the first portion of the period, 1904 to 2106Z, tops by satellite averaged 0.5 km above the radar and ESI's both by $\overline{B}_N + \overline{IR}$ and $H_{\overline{IR}}$ alone averaged about 0.7 above those by radar. The RMSE was 1.3 to 1.4 ESI_p. During the second period, tops by satellite averaged 1.1 km lower than the first period. Aircraft reports, although not exactly over the sample area, also showed a decline in top altitude; however, the average radar tops rose 0.1 km from the first to the second period. This may be attributed to echoes received by the lower side lobe of the antenna pattern being misidentified as higher echoes in the main lobe. ESI_p values by radar were much higher than those by satellite during the second period. Examination of the mass profiles shows that this is only partially due to the side lobe effect because very high water content was found below 3 km, the freezing level. The cause for these large differences is not known nor do we know how often this occurs since the sample is small.

Availability of visible data through the second period might very well have raised the satellite estimates of ESI_p but they would still be less than ESI_p estimates by radar.

Table 13. Comparison of ESI_p Estimates from GOES-East Satellite and from SPANDAR Radar

Predictors and Times	n	Cloud Tops (km)		ESI_p Averages		ESI_p
	Number of Cases	Radar	Satellite	Radar	Satellite	rms Difference
$\overline{B}_N + \overline{IR}$ (1904 to 2106 Z)	23	8.6	9.1	1.9	2.7	1.4
$H_{\overline{IR}}$ (1904 to 2106Z)	23	8.6	9.1	1.9	2.5	1.3
$H_{\overline{IR}}$ (2203 to 2304Z)	15	8.7	8.0	7.0	1.8	6.0
$H_{\overline{IR}}$ (1904 to 2304Z)	38	8.6	8.7	3.9	2.2	3.9

60

5.3.2   TRADEX RADAR vs GOES-WEST SATELLITE— 8 JULY 1977

This comparison was made near Kwajalein Atoll through clouds at the northern edge of an Inter Tropical Convergence Zone cloud system. ESI_p values were computed along an RHI obtained at 0210Z on the 120° radial from the TRADEX radar. Mr. C. N. Touart read reflectivities by eye from a photograph of the color-contoured RHI display.   Profiles of mass at 1 km intervals were calculated and ESI_p values obtained.   Figure 24 compares these values with ESI_p derived from GOES-W, which scanned the area at 0223Z.   The 41 case equation with variables $\overline{B}_N$ and $\overline{IR}$ was used to calculate ESI_p.   The GOES navigation at this time was good to about 54 km.   The variation of radar values along the radial and the variation of the satellite contours match well.   The maximum of 4.1 on the RHI was in a shower area while the minimum of 1.2 occurred with cloud between 8 and 12 km.   The maximum of 3.8, found furthest from the radar, had a radar horizon near 8 km, but showers probably fell to the ocean.   Adjustments were not applied for the missing layer from the radar horizon to the sea, but if they had a slight increase would occur at the maximum of 4.1 and probably a significant increase at the maximum of 3.8.

It should be remembered, as noted in Section 2, that under these satellite viewing conditions a cloud 12 km high is positioned about 24 km too far to the west.   This case improves the comparison by placing the higher radar values even closer to the higher satellite values.   The comparison is considered good, especially in view of the uncertainties noted.

5.4   Aircraft vs Satellite ESI_p Values Near Kwajalein

5.4.1   THE 8 AUGUST 1976 CASE

This was a case of a small isolated shower, with anvil, but without secondary clouds.   The observational data were excellent.   The Kwajalein WSR-57 radar data, which showed other isolated showers, could be used to precisely locate the satellite data.   In addition to good 1-D PMS aircraft data during ascent and descent. excellent time lapse and still photography made it possible to develop detailed plots of cloud positions and shapes.   The cloud underwent a minimum of change during the soundings.   It drifted slowly, shear was weak, and mass measurements were essentially the same during ascent and descent.

61
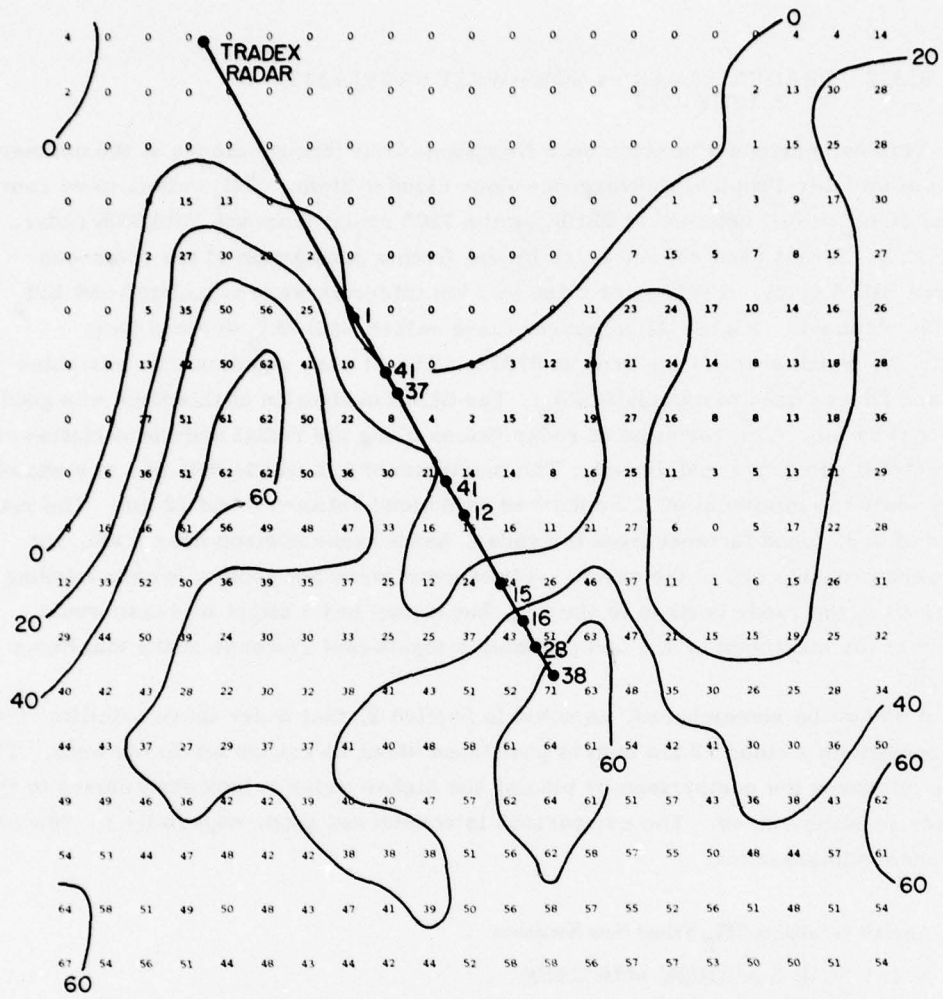
Figure 24. ESI$_p$ (in tenths) Derived from GOES-W. Each digit represents a rectangular area 8 km N-S by 15 km W-E (left - right). ESI$_p$ (in tenths) calculated from the TRADEX radar is shown along the radar radial

The cloud appeared to be "pumping", that is, one cell after another grew vertically and spread at upper levels. The spreading levels are shown in Figure 25, a photograph from the 8.0 km level. The full vertical extent of the cloud is depicted in cross section along the aircraft track in Figure 26. Precipitation nearly evaporated by the time it reached 2 or 3 km altitude only to be replaced by another growing cell. Principal aircraft penetrations were in the 4.5 to 6.0 km, 9.2, and 12.8 km levels. By interpolation between levels and the use of visual clues, mass profiles were generated for the core of the cloud and several distances out from the core. These profiles are also shown in Figure 26. From these ESI$_p$ was calculated.

62

Figure 25. Cumulonimbus Anvil Showing Two Levels of Spreading Below the Top. Taken from 8.0 km MSL, about 7 km distant. 1-D probes show on the front of the aircraft
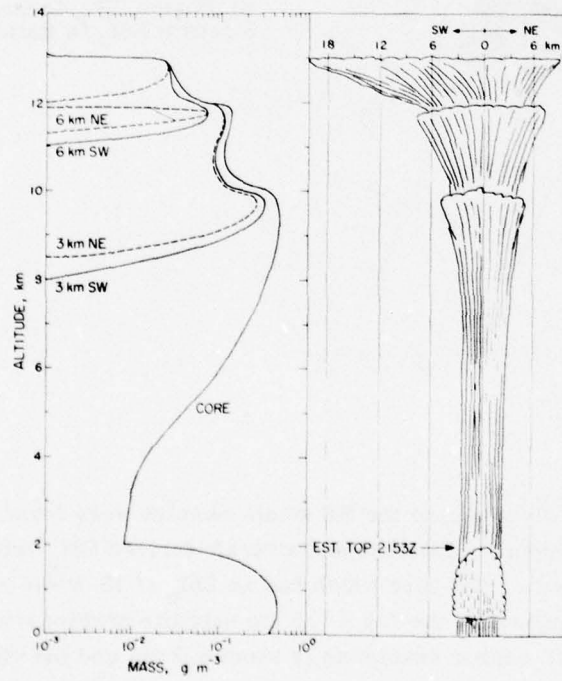

Figure 26. Left: Mass Profiles, at the Storm Core, 3 and 6 km NE and SW from the Core Along the Aircraft Track, Right: Cross Section of the Storm Along the Aircraft Track

63

The satellite data mesh, radar echoes, aircraft track and ESI_p values were then mapped and superimposed as shown in Figure 27. Satellite $\overline{B}_N$ and $\overline{IR}$ data from the NOAA 4 satellite for each square were used to compute ESI_p as shown using the 41 case equation.
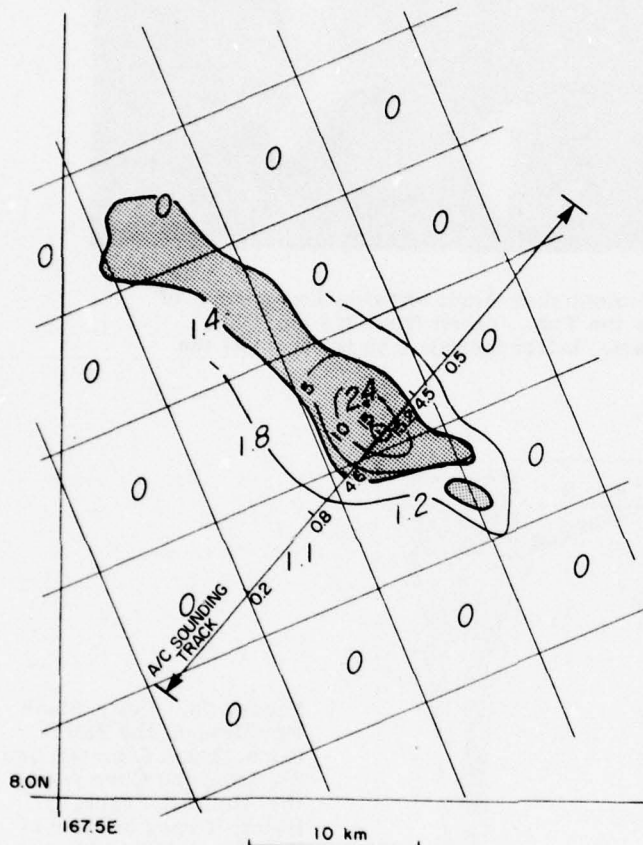

Figure 27. WSR-57 Radar Echo (stippled) of the Storm at Satellite Pass Time, ESI_p Values Along the Aircraft Track and Estimated ESI_p Contours. Satellite ESI_p In italics

In the SW the anvil lay over clear air; to the NE small cumulus were found under the anvil. Agreement between the satellite and aircraft derived ESI_p values is good over both areas of the anvil. The core which had an ESI_p of 15.2 was estimated to be only 2 km wide as opposed to the 7.5×7.5 km satellite archive mesh. For this viewing geometry, the IR sensor resolution is about 8.2 km and the visible resolution is half that size so these could not be expected to characterize the core of the storm. The satellite archive square which contained the storm core had an

64

ESI_p of 2.4 while the average of the aircraft ESI_p contours over that square was about 5.5 ESI_p. Thus the average ESI_p was 2 times the satellite estimate while the core ESI_p was 6 times the satellite estimate. Table 14 summarizes the comparisons. Satellite estimates for adjacent squares were weighted for comparison to aircraft estimates in between squares.

Table 14. ESI_p Determined by Aircraft and by Satellite in Relation to the Core of a Small Isolated Cumulonimbus Cloud

Location	Satellite	Aircraft
Shower core	2.4	15.2
3 km NE, edge of precip.	2.0	4.5
6 km NE, some ci, cu below	0	0.5
3 km SW in precip.	1.7	4.6
6 km SW anvil only	1.1	0.8
12 km SW anvil only	0.5	0.2
Brightest and coldest (combined adjacent sat. squares)	2.9	---

5.4.2 THE 12 AUGUST 1976 CASE

In this case the cloud system was more complicated than the 8 August 1976 cloud system. The cloud sampled was a dying Cb whose base was about 6 km altitude. It was located on the northern edge of a cluster of Cb's of which two were active with heavy showers. The Lear aircraft PMS-1D and photography were good. A happenstance photo of the aircraft radar display proved vital when compared with the WSR-57 radar data to verify a cloud position.

The mass profile shown in Figure 28 was a smoothed fit of observed densities to give what was considered to be the most representative profile through the sounding area. From this an ESI_p of 4.7 was calculated.

A printout of ESI_p values, their contours, and WSR-57 radar echoes is shown in Figure 29. The ESI_p values were calculated from NOAA 4 satellite data using the 41 case equation. The racetrack sounding area of the aircraft is enclosed in a box-like area near 10N, 168E. Average ESI_p within this box is 4.6, a value very close to that calculated from the aircraft data.
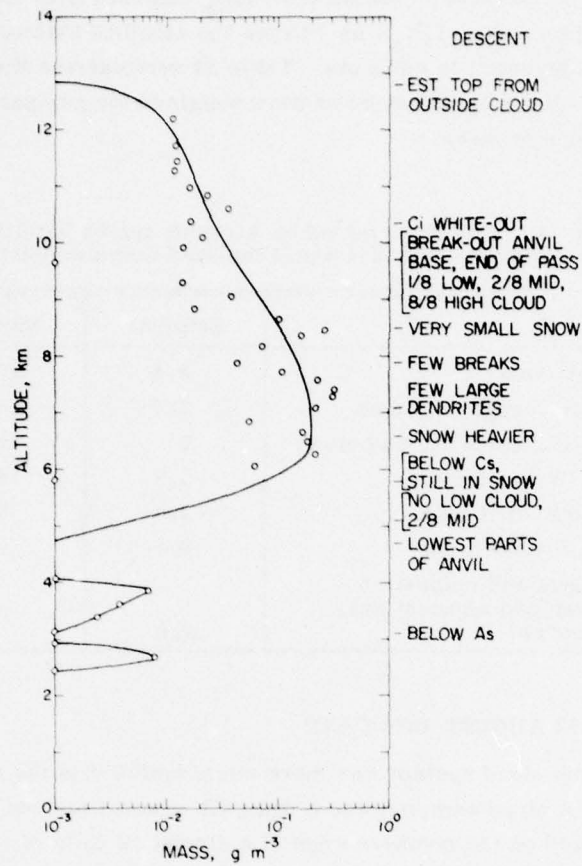
Figure 28. Mass Profile and Observer Notes Through
Dying Cumulonimbus (Cb) Near Kwajalein on 12 August
1976. Points are PMS-1D system measurements

Comparison of the WSR-57 radar echoes based on beam scans at 0° elevation
and the ESI_p contours is of interest. In the sample area no echo was seen. The lack
of echo is reasonable since the aircraft observed no low precipitation with the com-
plete loss of virga at 4.8 km. The echo near 9.5N and 167.5E conforms quite well
with heavy satellite ESI_p except to the north where it covered some ESI_p values of
zero. In that area $\bar{B}_N$ was as low as 38 and the IR temperature as high as 286°K.
At this range of 110 km from the radar, the beam would not see the lowest altitudes
and therefore could not detect rain from low cumulus. More likely, the echo was
from virga with little or no cloud below 3 km. It was obviously quite transparent
to the IR and not very reflective in the visible. Near 9.0N, 168.0E a portion of

66

another echo is found in an ESI_p area of zero. These clouds had a $\overline{B}_N$ of 50 to 93 while the $\overline{IR}$ was as low at 271°K. The echo here, only 40 km from the radar, was most likely due to rain from cumulus that were not quite bright or cold enough to give an ESI_p above zero according to the general equation. In another area just to the northwest no echo was observed where the satellite ESI_p was 10. These observations show the difficulties of comparing ESI_p satellite values with areas of radar echo seen only in a horizontal plane.
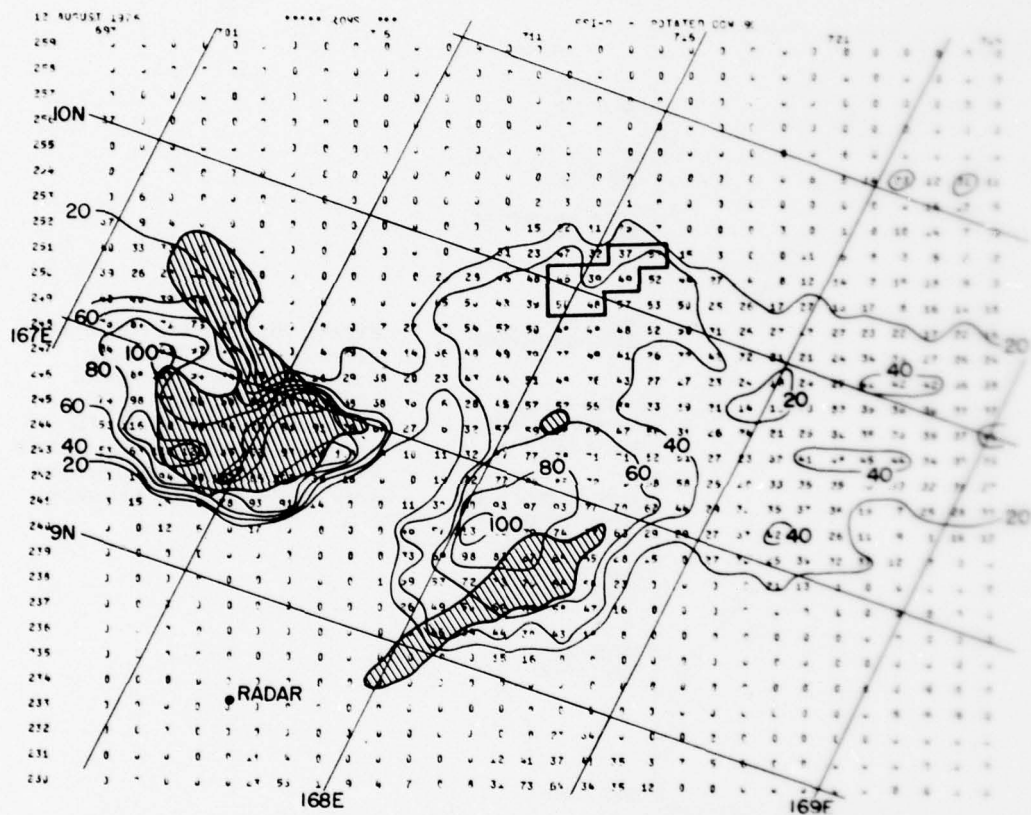

Figure 29. ESI_p (in tenths), WSR-57 Radar Echoes (stippled) and Aircraft Sounding Area (heavy box) on 2143Z 12 August 1976

5.4.3 THE 14 AUGUST 1976 CASE

In this case, the cloud sampled was an active shower having a top at 13 km with rain to the ocean surface. A racetrack aircraft ascent was made along the 157° (true) radial from Kwajalein. The southern end of the track was inside the cloud. The northern end of the track, during ascent, was often outside the cloud wall except in the altitude range of 9 and 13 km where cloud extended north of the flight track.

67

Particle classification was made from the PMS-2D samples. PMS-1D mass estimates were then computed and plotted as shown in Figure 30. Observer notes are appended. The solid profile line is intended to represent the mean mass over a N-S distance of about 22 km or three satellite grid squares. An ESI_p of 11.6 was calculated from this profile.
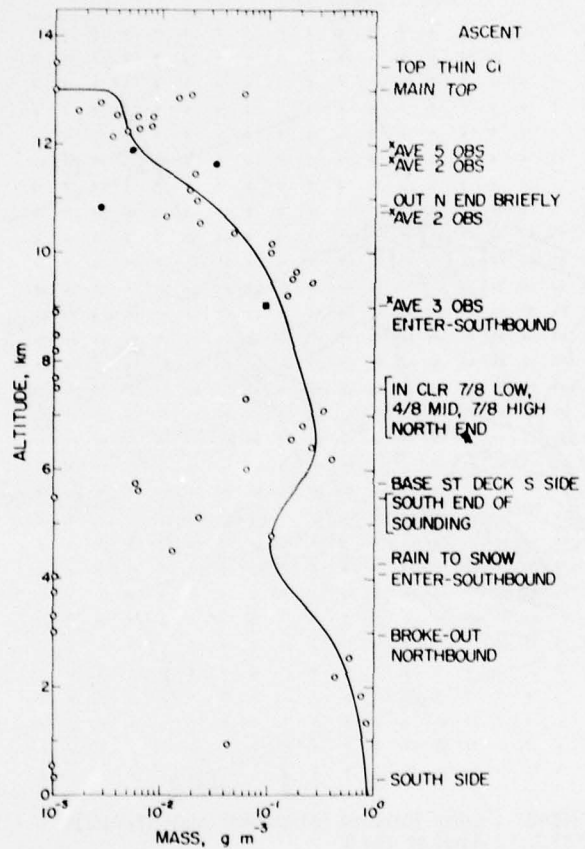

Figure 30. Mass Profile and Observer Notes Through Active Cb Near Kwajalein, 2103 to 2142Z, 14 August 1976. Points are PMS-1D system measurements. Points with crosses (x) are averages over more than one sampling run

Unfortunately, the NOAA 4 satellite data could not be positioned relative to the aircraft with certainty. The Kwajalein WSR-57 radar data were used to make the adjustment. Isolated echoes to the SSE and NNE of the radar were matched to apparent cloud centers in the satellite data. The resulting best fit of the satellite data and radar patterns is shown in Figure 31. Radar pictures at 15-min intervals showed that the echoes were moving from 162° at 33 km hr^{-1}. In spite of careful

68

pattern interpolation during the sounding period, 2104 to 2142Z, few echoes were found where the aircraft was supposed to be sampling. Some uncertainty remains since larger echoes are expected from such a vigorous cloud system.
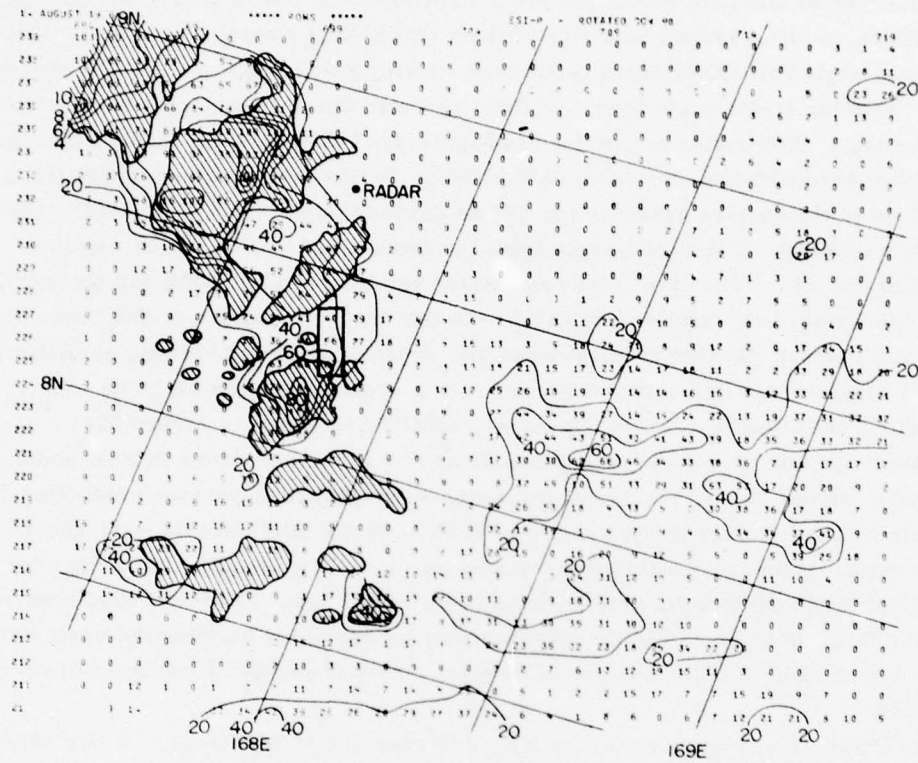

Figure 31. ESI_p (in tenths), WSR-57 Radar Echoes at 2131Z (stippled) and Aircraft Sounding Area (heavy box). Satellite data at 2138Z 14 August 1976

Average ESI_p over the three satellite squares is 5.4 or about half the value found by aircraft. On the other hand, if the aircraft sounding was located in the same size area but one square to the left and two squares down an average of 7.8 is found.

5.5   Effect of Slant Viewing from a Satellite

Reference was made in Section 4.6 to the utility of the GOES-West satellite data for delineating areas of significant ESI_p in the Kwajalein area. The GOES-West satellite views Kwajalein from an angle of 65° off vertical. Hence, the atmospheric path from Kwajalein to GOES-West is more than twice as great as the path to a

69

satellite directly overhead and atmospheric attenuation of reflected sunlight or terrestrial emission could be significantly greater for the longer paths. Tests were conducted to insure that the ESI_p prediction equations were useful for high viewing angles. An example is shown here to illustrate the effects of extreme slant viewing.

In order to simulate conditions when the Kwajalein area is viewed for planning operations, a cloud system was viewed from GOES-East looking westward at about the same angle that GOES-West looks when viewing Kwajalein. A time was chosen when the solar zenith angle from the cloud was also about the same as during operational usage. The angles are defined in Figure 4. The view from GOES-East was then compared with the view from GOES-West. In this test the zenith angle from the cloud to the eastern satellite was 56° as opposed to 65° from Kwajalein to the western satellite. The zenith angle from the same cloud system to the western satellite was 17°. The view from the eastern satellite was at 1600Z and the view from the western satellite was at 1615Z. In this test, the pattern of ESI_p computed from the western satellite is considered ESI_p truth since it had viewing conditions close to those in the development sample. It is shown in Figure 32. The ESI_p pattern as seen slantwise from the eastern satellite is shown in Figure 33.

Most obvious in comparing Figures 32 and 33 is the difference in E-W scale. Secondly, clouds viewed slantwise are displaced westward a distance proportional to their height. Clouds in the vicinity of 8.5N, 124.0W in Figure 32 were about 13 km high. If the top western edge was sharp, simple geometry places the edge 20 km further west than its true position in the slant view. Observed displacement is about 0.4° or 44 km. The discrepancy may be due to not knowing the exact nature of the cloud edge, that is, how far did the anvil extend westward and how diffuse was the edge.

In Figure 32, a large area with ESI_p less than 1.0 is northwest of a line between 8.0N, 122.3W; and 7.3N, and 123.0W. In the slant view, Figure 33, the same area tends to have ESI_p slightly above 1.0 with many fewer zeros. On the other hand, areas of high values are similar from both angles. For example, the area greater than 4.0, centered near 8.5N, 123.8W in Figure 32 is about the same in size in the slant view of Figure 33. Peak values are 6.2 vertical vs 5.4 slantwise. Near 9.8N, 122.2W peak values are 10.0 vertical vs 7.7 slantwise.

Of course a comparison of this type assumes correct calibrations of both the visible and IR on both satellites and proper normalization factors for the sun angles. The calibrations were tested by simultaneous view of the same cloud located near the equator and mid-way between the satellites when the sun was at local noon. These comparisons suggest that the calibrations do not yield strictly compatible data. GOES-EAST IR temperatures appeared to be about 5° lower than GOES-West at 200°K and 1° lower at 290°K. Calibrated brightness of GOES-East averaged 2 percent higher than Goes-West with no discernible trend between high and low values.

70
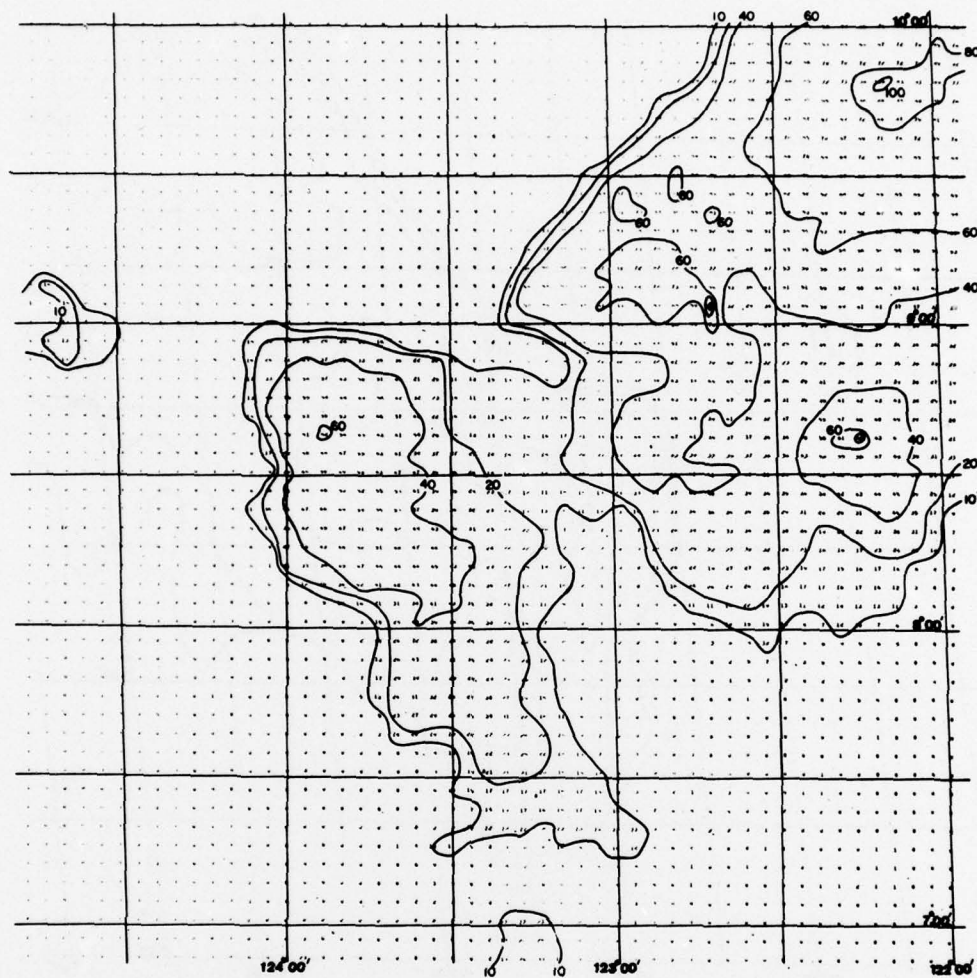
Figure 32. ESI$_p$ (in tenths) Pattern Calculated from GOES W. 17° Zenith Angle to Satellite. 1615Z 25 July 1977

In summary, the slant view gave ESI$_p$ about 20 percent too low where a more or less uniform field of high (3 to 10) ESI$_p$ was observed. Where the cloud elements were small and did not fill the sensor field of view in the slant view, the ESI$_p$ values were low. This condition can be detected in the slant view by a few isolated small ESI values. Widespread small values of ESI$_p$ in the slant view were probably a field of broken clouds or layer of thin clouds and the ESI$_p$ values were higher than those in the vertical view.

71
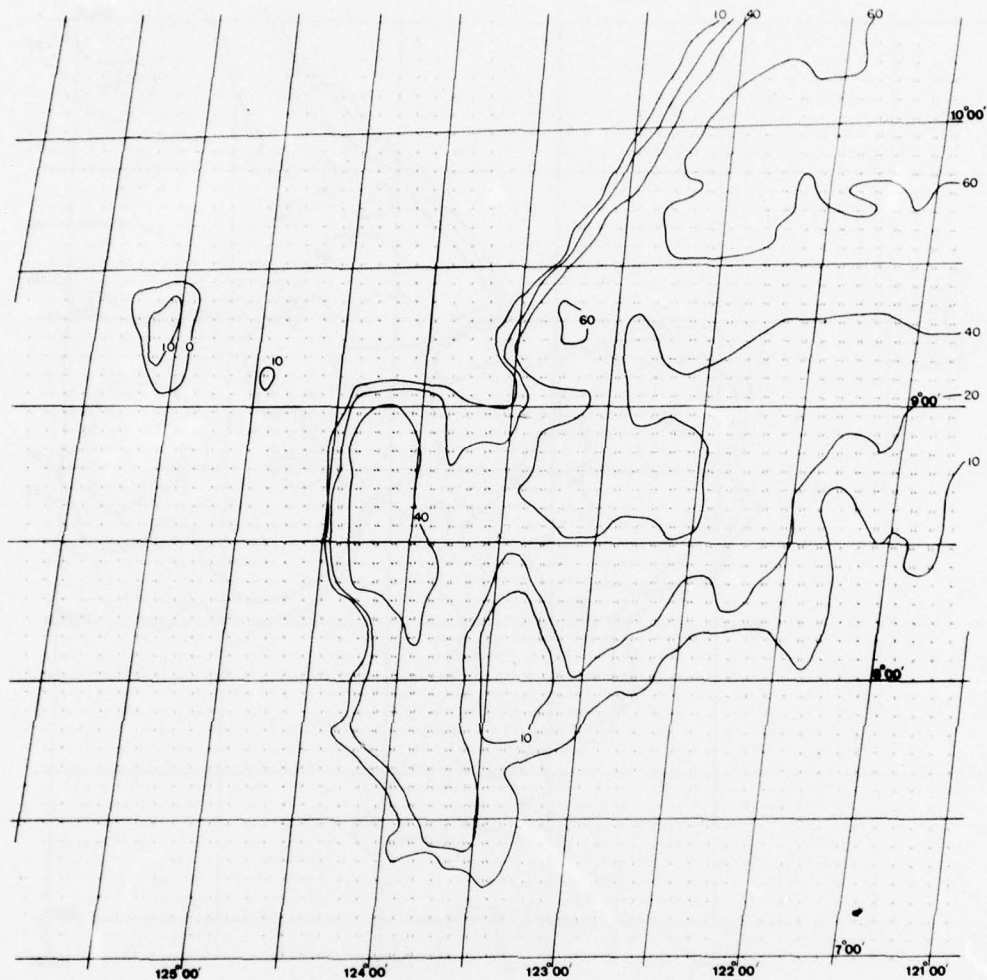
Figure 33. ESI_p (in tenths) Pattern Calculated from GOES E, 56° Zenith Angle to Satellite. 1600Z 25 July 1977

5.6 Satellite vs AFGL-II Erosion Estimates

Satellite Estimates of ESI_p were compared to ESI_p estimated from the AFGL II model discussed in Section 1.2. The comparison is made possible by the fact that AFGL II hydrometeor profiles were provided every three hours. Therefore, once per day satellite estimates over the 11 AFGL II stations could be compared to the AFGL II estimates closest in time and always be within 1.5 hr of AFGL II estimates. As in earlier applications over Europe and Asia, the satellite estimates

72

were based on averages of 5×5 arrays of data points representing areas of about 50×50 km. The arrays were centered as close as possible to the AFGL II station locations. The two climatologies had an overlapping period of April 1973 to January 1974 . May, July, October, and January were chosen as representative seasonal months and comparisons were made for all 11 stations for all the days of those months. The maximum number of pairs to compare would be 1364; however, only 1113 were found due to missing satellite data for some dates and locations. In the months May, July, and October, satellite estimates of ESI_p were from the $\overline{IR} + \overline{B}_N$ equation while in January they were from the $H_{\overline{IR}}$ equation.

ESI_p values were also calculated from the AFGL II hydrometeor profiles using two different methods. Two methods are available since the AFGL II model provides not only estimates of hydrometeor mass densities but also estimates of the percent horizontal coverage of cloud and precipitation layers. In the first method, hydrometeor density was simply multiplied by the fraction of horizontal coverage before ESI_p values were calculated. These ESI_p values represent areal averages and can be compared directly to the satellite estimates which are also areal averages. In the second method, ESI_p values were calculated assuming that all cloud layers had 100 percent coverage. These values describe the worst case situation of a reentry vehicle encountering clouds at all the cloud layers. These values can be compared to the satellite estimates if the satellite estimates are increased by the ratio of the Method 2 ESI_p divided by the Method 1 ESI_p. For either method, AFGL II ESI_p values before and after the satellite pass time were linearly interpolated to the time of the satellite pass before comparison to the satellite values.

Exceedance statistics for AFGL II and satellite ESI_p values in four months combined are compared in Figures 34 and 35. The plotted lines give the percentages of time when ESI_p thresholds are exceeded. The percentage of exceedance decreases as ESI_p increases. Figure 34 has the results for Method 1, in which reduced AFGL II values are compared to satellite values. AFGL II percentages are greater than satellite percentages for ESI_p values of 2 and greater. Inspection of plots for individual months revealed a general tendency for greater AFGL II percentages above an ESI_p value of 2 with the extreme differences in the month of July. A definitive explanation of the July differences is lacking although two possibilities clearly exist. First, the 50×50 km averages of satellite data may not properly represent the convective weather of July and thereby underestimate ESI_p as discussed in Section 5.4.1. On the other hand, the second possibility is that the AFGL II data include surface reports of cloud coverage which overestimate the layer coverage of convective clouds since the observer estimates of sky coverage tend to combine bases and sides.

73
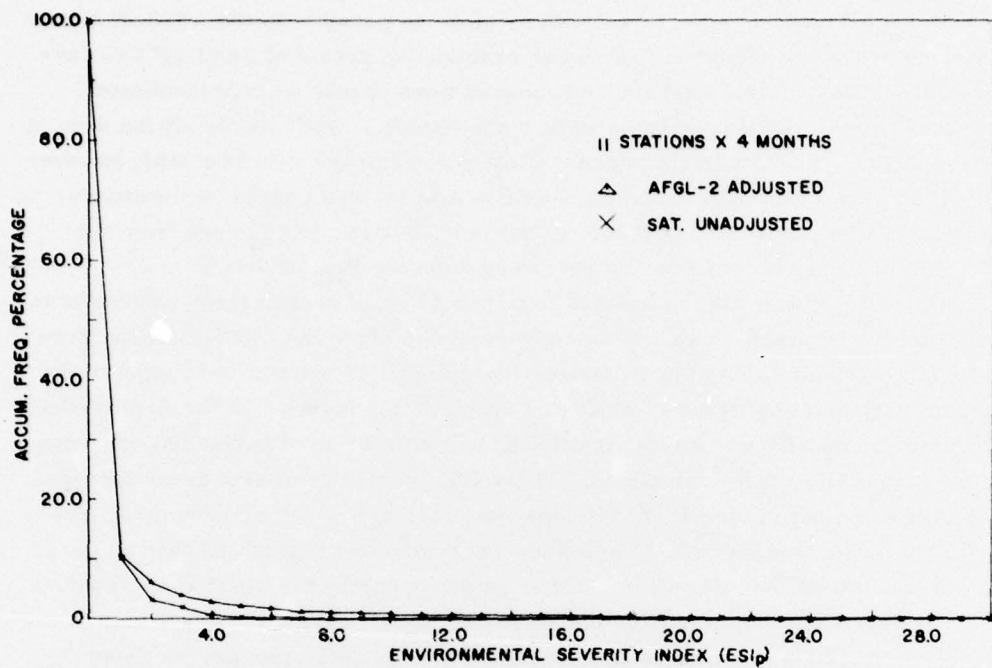
Figure 34. Method 1 Exceedance Statistics for AFGL II and Satellite ESI_p Values. AFGL II values are reduced according to Method 1 (see text), satellite values are unchanged

Figure 35 has the results for Method 2, in which maximum AFGL II values of ESI_p are compared to increased values from the satellite. The percentages are moderately higher than the corresponding Method 1 percentages. In Figure 35, AFGL II percentages are remarkably close to the satellite percentages for ESI_p thresholds of five or less. For six and above AFGL II percentages are higher, as they were in Method 1.

These comparisons are considered to be good, taking into account that the satellite and AFGL II estimates are from two completely different approaches each with substantial uncertainty.

74
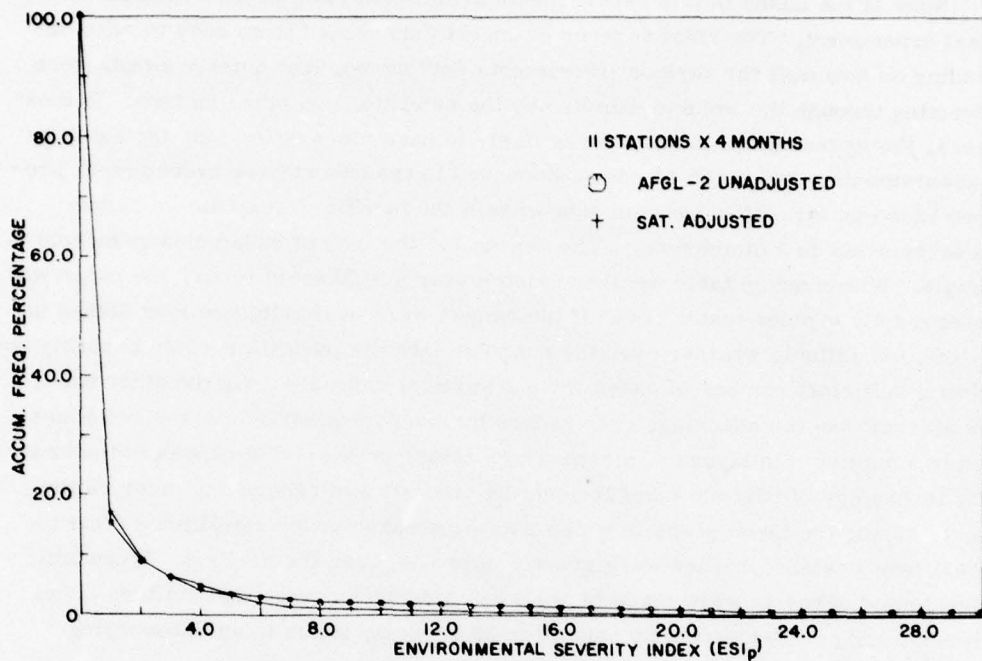
Figure 35.   Method 2 Exceedance Statistics for AFGL II and Satellite ESI$_p$ Values. Satellite values are increased according to Method 2 (see text), AFGL II values are unchanged

5.7   Conclusions on Verification

An ideal experiment for verification of the erosion estimates from satellites would have the following elements. First, one or more aircraft would be available for rapid ascents and descents to measure particle size distributions and phase as a function of altitude and sufficient for numerical models of reentry vehicle erosion. Then, in order to bridge the gap between the very small volumes sensed from aircraft and the large volumes sensed from satellites, active systems such as radars or lidars would scan the volume sensed by the satellite. Moreover, the satellite measurements would be calibrated to precise physical standards which could be updated at the time of cloud observations. The satellite measurements would be precisely navigated and colocated with the other observations. Given these capabilities, simultaneous observations of clouds would be taken in a great number of cases for different cloud types, thicknesses, coverages, rainfall rates, temperature profiles, sun and observation angles, etc. Given these data, relationships between satellite measurements and erosion parameters could be checked with confidence.

75

None of the cases in this report meets all or even most of the elements of the ideal experiment. The chief sources of uncertainty varied from case to case depending on how well the various instruments performed, how quickly clouds were advecting through the volume sampled by the satellite, and other factors. In most cases, the hydrometeor profiles were likely to have more error than the satellite measurements. All of the 41 cases discussed in the report have hydrometeor profiles based on aircraft measurements without the benefit of quantitative radar measurements in 3 dimensions. The reason for the lack of radar measurements is simple. Whenever suitable weather existed over a calibrated radar, the range was reserved for erosion tests. Even if the ranges were available, the long delays in waiting for suitable weather over the range at satellite pass time would probably not allow a sufficient number of cases for a statistical approach. On the other hand, the aircraft has the advantage over radars by measuring particle sizes and phases, and in sampling thin layers of cirrus which return undetectable echoes to the radar. The technology of particle measurement by aircraft was undergoing many refinements during the three years in which data were taken under satellites so that the latest hydrometeor profiles were greatly improved over the earliest. When both ascents and descents were made by the Lear aircraft in large mid-latitude cloud systems, ESI_p values varied by only 20 to 30 percent, which is an encouraging number.

The satellite instruments appear to have reasonably small errors according to Conlan. [18] This claim is not surprising since the satellite instruments were an operational series which was not undergoing development changes. When the rms error of 2.02°K in the satellite IR temperature is introduced in Eq. (1) of Table 6, the corresponding ESI_p error is only 0.33 or 6 percent in the worst of 41 cases. Similar errors were found converting temperature to altitude (Table 14). Visible data are subject to greater uncertainty due to corrections for solar illumination and bidirectional reflectance; however, this uncertainty is minimized by the fact that visible data are weighted much less than IR data in the erosion prediction equations. No allowance was made for background brightness or temperature, which is a source of uncertainty for thin clouds or partial cloud coverage.

The errors in earth location of satellite data introduce uncertainty which may exceed the instrumental error for some cases. Despite procedures to adjust the archive mapping some uncertainty remains as to the exact boundary of satellite data suitable for comparison to the aircraft profiles and leads to uncertainty in the areal averages of the satellite data. The uncertainty increases when satellite data are averaged over smaller areas. Compared to the satellite, aircraft navigation was excellent and generally needed no adjustment.

The uncertainty in applying prediction equations developed over 70×70 km averages of satellite data in temperate latitudes to tropical cloudiness near

76

Kwajalein was tested in three cases. For these, the maximum resolution data of 7.5×7.5 km from the NOAA archive were used to better characterize the fine-scale cloudiness. In the case of a very small central storm core which reached the surface the satellite underestimated the core ESI_p by six times. Estimates through thin portions of the anvil were in close agreement. In the case of a large dying shower cloud whose virga only reached downward to about 6 km MSL, satellite estimates were close to the aircraft measurements. A third case must be viewed with uncertainty due to navigational problems. This cloud was deep and active with rain reaching the surface. The satellite estimates were from 50 to 60 percent of the A/C estimates. These tests indicated that reasonable values of ESI_p are given by the prediction equation when maximum resolution data are used without averaging.

For all of the erosion parameters, ESI_p, ΔS, ADI, and ΔR, multiple regression correlation coefficients in the range of 0.7 to 0.8 were consistently found from the sample of 41 cases. The coefficients imply that a highly significant 50 to 65 percent of the sample variance is explained by the equations. When the 41 case sample was randomly divided into two samples, quite similar prediction equations were found for each sample. Therefore, we do not expect that larger samples or a repeat of the experiment would change the correlation by much. We do not claim to have climatologically representative numbers of cloud types in our sample, that is, we are probably underrepresented in cirrus cases and overrepresented in multilayer and thick cloud systems. On the other hand, samples and tests have been made over a great range of cloud conditions observed by aircraft and infrared and visible measurements by satellites. Finally, the basic relationship between satellite measurements and erosion estimates has held up remarkably well in a variety of tests. Properly calibrated data from GOES geostationary satellites has been sub-stituted for data from NOAA polar orbiting satellites with no noticeable loss of usefulness. Satellite estimates of erosion have compared well with estimates from such varied sources as aircraft sampling, radar mapping, and human interpretation of surface weather reports and radiosonde data.

77

References

1. Smith, R.C., Capt (1974) Atmospheric Moisture Parameterization, USAFETAC TN 74-1, Washington, D.C. 19 pp.

2. Feddes, R.G., Capt (1974) A Synoptic-scale Model for Simulating Condensed Atmospheric Moisture, USAFETAC TN 74-1, Washington, D.C., 21 pp.

3. Cunningham, R.M., and Peirce, R.M. (1974) Environmental Definition Plan Cross Section Analysis, AFGL (unpub. ms.).

4. Feteris, P.J., Lisa, A.S., and Bussey, A.J. (1975) Environmental Definition Program Cross Sectional Analysis; Summary of Data and Analysis Techniques, AFCRL-TR-76-0002. Final Rept. F19628-74-C-0073, Environmental Res. and Tech., Inc., Concord, Massachusetts 01742, 34 pp.

5. Gringorten, I.I. (1976) Areal Coverage Estimates by Stochastic Modeling, AFGL-TR-76-0148, ERP No. 573, 56 pp.

6. Liou, K-N, and Stoffel, T. (1976) Remote Sensing of Cirrus Cloud Compositions From Satellites, AFGL-TR-76-0027, 81 pp, University of Utah, Salt Lake City, Utah 84112.

7. Feddes, R.G., and Liou, K-N (1977) Cloud Composition Determination by Satellite Sensing Using the Nimbus VI High Resolution Infrared Sounder, AFGL-TR-77-0123, 140 pp, University of Utah, Salt Lake City, Utah 84112.

8. Staelin, D.H., Kunzi, K.F., Pettyjohn, R.L., Poon, R.K.L., and Wilcox, R.W. (1976) Remote sensing of atmospheric water vapor and liquid water with the Nimbus 5 microwave spectrometer, J. Appl. Meteor. 15:1204-1214.

9. Wilheit, T.T., Chang, A.T.C., Rao, M.S.V., Rodgers, E.B., and Theon, J.S. (1977) A satellite technique for quantitatively mapping rainfall rates over the oceans, J. Appl. Meteor. 16:551-560.

10. Booth, A.L. (1973) Objective cloud type classification using visual and infrared satellite data, Proceedings of the 3rd Conf. on Probability and Statistics in Atmospheric Science, pp 220-227.

11. Shenk, W.E., Holub, R.J., and Neff, R.A. (1976) A multispectral cloud type identification method developed for tropical ocean areas with Nimbus-3 MRIR measurements, Mo. Wea. Rev. 104:284-291.

79

12. Reynolds, D., and Vonder Haar, T.H. (1973) A comparison of radar-determined cloud height and reflected solar radiance measured from the geosynchronous satellite ATS-3, J. Appl. Meteor. 12:1082-1085.

13. Griffith, C.G., and Woodley, W.L. (1973) On the variation with height of the top brightness of precipitating convective clouds, J. Appl. Meteor. 12:1086-1089.

14. Kaveney, W.J., Feddes, R., and Liou, K-N (1976) Statistical Inference of Cloud Thickness from NOAA 4 Scanning Radiometer Data, AFGL-TR-76-0105, 76 pp, University of Utah, Salt Lake City, Utah 84112.

15. Martin, D.W., and Scherer, W.D. (1973) Review of satellite rainfall estimation methods, Bull. Amer. Meteor. Soc. 54:661-674.

16. Griffith, C.G., Woodley, W.L., Grube, P.G., Martin, D.W., and Stout, J. (1977) Rain Estimation from Geosynchronous Satellite Imagery, Visible and Infrared Studies, submitted to Monthly Weather Review from NHEML, NOAA, Coral Gables, Florida.

17. Bunting, J.T. (1976) Cloud Properties from Satellite Infrared and Visible Measurements, AFGL-TR-76-0287, 6 pp.

18. Conlan, E.F. (1973) Operational Products from ITOS Scanning Radiometer Data, NOAA Technical Memorandum NESS 52, 57 pp.

19. Sikula, G.J., and Vonder Haar, T.H. (1972) Very Short Range Local Area Weather Forecasting Using Measurements from Geosynchronous Meteorological Satellites, Final Report for Contract F19628-71-C-0073, AFCRL-76-0260.

20. Raschke, E., Vonder Haar, T.H., Pasternak, M., and Bandeen, W.R. (1973) The Radiation Balance of the Earth-Atmosphere System from Nimbus 3 Radiation Measurements, NASA TN D-7249, 71 pp.

21. Cozzens, D.E. (1974) Technique to Earth Locate and Analyze Data from Satellite Sensors, pp 13-36. Burke, L. (1974) Met and Math. Anal. Final Rept. Regis College, AFCRL-TR-74-0558.

22. Bristor, C.L. (1975) Central Processing and Analysis of Geostationary Satellite Data, NOAA Tech Mem. NESS 64, Washington, D.C., 155 pp.

23. Church, J.F., Lt Col, Pocs, K.K., and Spatola, A.A. (1975) The Continuous Aluminum-Foil Hydrometeor Sampler; Design, Operation, Data Analysis Procedures, and Operating Instructions, AFCRL-TR-75-0370, 70 pp.

24. Plank, V.G. (1974) Hydrometeor Parameters Determined from the Radar Data of the SAMS Rain Erosion Program, SAMS Rept. No. 2, AFCRL-TR-74-0249, 86 pp.

25. Hobbs, P.V., Radke, L.F., and Atkinson, D.G. (1975) Airborne Measurements and Observations in Cirrus Clouds, AFCRL-TR-75-0249, Sci. Rept. No. 1, University of Washington, Seattle, Washington, 117 pp.

26. Berthel, R.O. (1975) A Climatology of Selected Storms for Wallops Island, Virginia, 1971-1975, SAMS Rept. No. 4, AFGL-TR-76-0118, 32 pp.

27. Booker, R.D., and Windes, J. (1977) HAWADS Equipment Description and Operational Manual, Aeromet, Inc., AFGL-TR-77-0066, 115 pp.

28. Knollenberg, R.G. (1975) The Response of Optical Array Spectrometers to Ice and Snow: A Study of Probe Size to Crystal Mass Relationships, Sci. Rept. No. 1, Particle Measuring Systems, Inc., Boulder, Colorado 80301, AFCRL-TR-75-0494, 70 pp.

29. Knollenberg, R. G. (1976) The Response of Optical Array Spectrometers to Ice and Snow: a Study of 2-D Probe Area-to-Mass Relationships, Final Rept. Particle Measuring Systems, Inc., Boulder, Colorado 80301, AFGL-TR-76-0273.

30. Serbagi, R. C., Rodenhiser, P. M., and Kaplan, F. B. (1974) Warm Fog Dissipation Models and Control and Processing Programs for Airborne Data System, AFCRL-TR-74-0411, 164 pp, Digital Prog. Services, Inc., Waltham, Massachusetts 02154.

31. Belsky, L. E., Kaplan, F. B., and Rodenheiser, P. M. (1975) Development and Application of Data Processing Techniques and Analytic Procedure to Cloud Physics Data, AFCRL-TR-75-0427, 160 pp, Digital Prog. Services, Inc., Waltham, Massachusetts 02154.

32. Belsky, L. E., Francis, M. W., Kaplan, F. B., and O'Neil, J. E. (1976) Continuation of Development and Application of Data Processing Techniques and Analytic Procedures to Cloud Physics Data, AFGL-TR-76-0182, 198 pp, Digital Prog. Services, Inc., Waltham, Massachusetts 02154.

33. Spiegler, D. B., and Fowler, M. G. (1972) Four Dimensional World Wide Atmospheric Models (surface-25 km altitude) NASA CR-2082, Environmental Res. and Tech., Inc., Concord, Massachusetts 01742, 65 pp.

34. Crutcher, H. L., and Meserve, J. M. (1970) Selected Level Heights, Temperature and Dew Points for the Northern Hemisphere, NAVAIR 50-IC-52.

Computer Processing of Archived Satellite Data for
Climatological Applications

The production of erosion climatologies over target areas and test ranges required extensive computer programming and execution time. The same sequence of programs was used for each climatology. The only difference was the specification of a different box of rows and columns within the NOAA Northern Hemisphere satellite archive. For the Eurasian climatology, the box was large with 705 × 750 data points covering most of Europe and Asia. With arrays of this size, it was convenient to work with only 4 days at one time. For the test range climatologies, the boxes were much smaller with 20 × 25 data points covering impact areas near Kwajalein Atoll and Wallops Island, Virginia. With these smaller arrays, it was convenient to work with 8 days and both areas at one time.

The following list gives the titles and functions for programs to process archived NOAA satellite data to produce erosion climatologies. The NOAA archive was described in Section 2.1. An estimate of CP time on the AFGL CDC-6600 computer for the Eurasian climatology is given for the programs.

Program	Function
CORFACT	Determines orbits and calculates viewing angles for each 10 × 10 array of data for each day on the NOAA SR polar sterographic archive tapes. Selects appropriate correction factors for visible data from tables of bidirectional reflectance. (380 sec/day)

83

Program	Function
SRPACK	Unpacks data from SR archive tapes and saves data in predetermined boxes. Checks for bad records. (350 sec/day)
SRCORR	Merges data from 2 tapes to eliminate the "dateline" over Europe in the SR archive tapes and multiplies all visible data by appropriate correction factors. (500 sec/day)
SRESI	Averages visible and IR data over 5×5 arrays. Tests for bad or missing data. Output options are erosion parameter estimates. (170 sec/day)
SRESIP	Calculates estimates of ESI_p, ADI, ΔS, ΔR, and also total LWC from average visible and IR for summer months and IR and temperature profiles for winter months. (30 sec/day)
COZPT	Generates computer plots of areas where erosion parameters exceed certain thresholds. National boundaries, coastlines, and a latitude-longitude grid are plotted for reference. See Figure 2 of Annex. (30 sec/day)
PROBMP	Computes probabilities of exceeding erosion parameters at all locations for a given month. The probabilities are used to adjust for missing data. (5 sec/day)
TSTATS	Computes monthly exceedance statistics for erosion parameters at specific locations. (5 sec/day)

The sequence and interdependence of the above programs is illustrated in Figure A1.
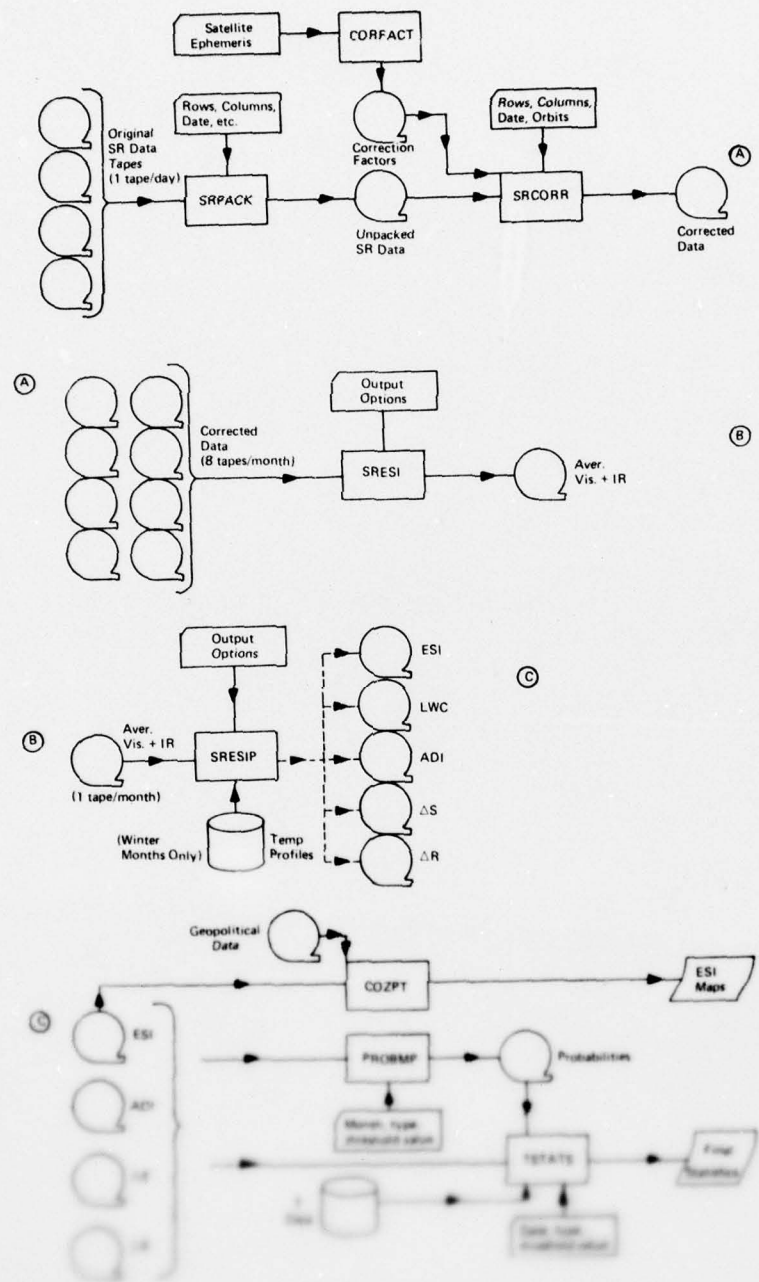
Figure A1. Sequence of Computer Programs Used to Produce Erosion
Climatologies and Maps from Archived Satellite Data.